Published in final edited form as:
IEEE Trans Terahertz Sci Technol. 2011 August 29; 1(1): 145–163. doi:10.1109/TTHZ.2011.2159546.

THz Dynamic Nuclear Polarization NMR

Emilio A. Nanni [Student Member, IEEE],
Department of Electrical Engineering and Computer Science, and the Plasma Science and Fusion Center, Massachusetts Institute of Technology, Cambridge, MA 02139 USA (enanni@mit.edu).

Alexander B. Barnes [Student Member, IEEE],
Department of Chemistry, the Francis Bitter Magnet Laboratory, and the Plasma Science and Fusion Center, Massachusetts Institute of Technology, Cambridge, MA 02139 USA (barnesab@mit.edu).

Robert G. Griffin, and
Department of Chemistry and the Francis Bitter Magnet Laboratory, Massachusetts Institute of Technology, Cambridge, MA 02139 USA (rgg@mit.edu).

Richard J. Temkin [Fellow, IEEE]
Department of Physics, and the Plasma Science and Fusion Center, Massachusetts Institute of Technology, Cambridge, MA 02139 USA (temkin@mit.edu).

Abstract

Dynamic nuclear polarization (DNP) increases the sensitivity of nuclear magnetic resonance (NMR) spectroscopy by using high frequency microwaves to transfer the polarization of the electrons to the nuclear spins. The enhancement in NMR sensitivity can amount to a factor of well above 100, enabling faster data acquisition and greatly improved NMR measurements. With the increasing magnetic fields (up to 23 T) used in NMR research, the required frequency for DNP falls into the THz band (140–600 GHz). Gyrotrons have been developed to meet the demanding specifications for DNP NMR, including power levels of tens of watts; frequency stability of a few megahertz; and power stability of 1% over runs that last for several days to weeks. Continuous gyrotron frequency tuning of over 1 GHz has also been demonstrated. The complete DNP NMR system must include a low loss transmission line; an optimized antenna; and a holder for efficient coupling of the THz radiation to the sample. This paper describes the DNP NMR process and illustrates the THz systems needed for this demanding spectroscopic application. THz DNP NMR is a rapidly developing, exciting area of THz science and technology.

Index Terms

Dynamic nuclear polarization (DNP); gyrotron; high power terahertz radiation; nuclear magnetic resonance (NMR); terahertz

I. Introduction

Nuclear magnetic resonance (NMR) is the preferred spectroscopic approach for the solution of problems in many areas of science, including physics, chemistry, biology, materials science, and medicine. The excellent resolution of NMR is a consequence of long nuclear

Color versions of one or more of the figures in this paper are available online at http://ieeexplore.ieee.org.

relaxation times that are in turn due to the small magnetic moments of the nuclear spins that couple weakly to the surrounding lattice. The small size of these magnetic moments, however, leads to reduced sensitivity in NMR experiments.

Dynamic nuclear polarization (DNP) increases the sensitivity of NMR by transferring the large spin polarization from stable paramagnetic centers to the nuclear spin reservoir [1]. In 1953, Overhauser [2] proposed that it was possible to transfer polarization to nuclei from electrons in metals by saturating the electron transition. This technique was experimentally verified by Carver and Slichter [3]. The DNP approach to NMR was extended to solid dielectrics by Abragam and Proctor [4] who first characterized the solid effect (SE). In the 1980's, Wind, Yannoni, Schaefer, and colleagues [5]–[7] performed DNP in conjunction with magic-angle-spinning (MAS) NMR.

Microwave driven DNP experiments are now recognized as powerful methods of enhancing signals in solid state and solution NMR and imaging. DNP improves the sensitivity of NMR spectra by about a factor of 100, thus reducing the acquisition time in multidimensional NMR experiments by roughly 10^4 [8]. This enhancement permits studies of larger molecules, reaction dynamics or high-throughput screening [9]. The theoretical maximum enhancement in the case of ^{1}H spins is given by the relationship $\gamma_S/\gamma_I \approx 660$ [2] where γ_S and γ_I are the electron and nuclear gyromagnetic ratios, indicating further developments to DNP methods and instrumentation should result in still higher enhancements. The power level desired from the THz source in DNP is highly dependent on several experimental factors including the mechanism of polarization, sample temperature, sample volume, polarizing agent and coupling efficiency of the source. Fundamentally, the power level needed is related to the electron relaxation rate which must be overcome in order to transfer polarization to the nucleus [10], [11]. Experimentally, the theoretical maximum enhancement from DNP is not achieved and is often limited by the available power.

These early, successful efforts in microwave driven DNP NMR could be extended to magnetic fields of up to about 3.4 T using commercially available sources, such as solid state multipliers, klystrons, etc., at a frequency of up to 94 GHz [12]. However, modern NMR spectroscopy has pushed to much higher magnetic fields, where much better spectral resolution is achieved. The extension of DNP NMR to high magnetic fields had to wait for the development of THz sources of radiation at the relevant frequencies. Fortunately, the development of the THz gyrotron enabled this extension of DNP NMR into the high magnetic field regime.

The first DNP NMR experiments using a gyrotron were conducted by Becerra *et al.* at the MIT Francis Bitter Magnet Laboratory at a magnetic field of 5 T, corresponding to 211 MHz NMR frequency and 140 GHz microwave frequency [13]. This successful advance was followed at MIT by extension of the technique to 9 T with the development of a 250 GHz gyrotron for use in a 380 MHz spectrometer [14] and later extension to 16 T with the development of a 460 GHz gyrotron for a 700 MHz spectrometer [15]. Research on the gyrotron also led to the discovery of broadband tuning of the gyrotron source, which could be useful in partially covering the electron spin resonance spectrum in DNP NMR experiments [15], [16].

As described by Griffin and Prisner in a recent article, DNP NMR is truly enjoying a "renaissance" at the present time [9]. Some examples of recently developed THz DNP NMR systems include a 260 GHz/400 MHz spectrometer in operation in Frankfurt, Germany [17], [18] and a 395 GHz/600 MHz spectrometer operating at the Osaka Institute in Japan [19]. Instrumentation for a 263 GHz/400 MHz DNP NMR system has been developed by industry and used in DNP NMR research [18], [20], [21].

This paper is organized as follows: in Section II, the THz DNP NMR technique is described in detail; Section III describes the source technology used in THz DNP NMR; Section IV describes the transmission lines for transporting the radiation from the source to the sample; Section V describes the sample probe, sample holder and the coupling of the THz power into the sample; Section VI is the summary and conclusions.

II. THz Dynamic Nuclear Polarization NMR

The structure and function of biomolecules are strongly correlated. Determining three-dimensional structural detail of proteins at an atomic resolution is crucial to understanding how they work as machines, catalyze chemical reactions, bind to each other, as well as how they interact with drugs and signaling molecules. By far, the most powerful technique available for structure determination is X-ray diffraction. However, there are certain drawbacks to X-ray crystallography; namely, the highly ordered crystalline environment required to record diffraction patterns is not a truly biological environment. In vivo, proteins are in solution, bound to or embedded inside the cellular membrane, intrinsically disordered, or arranged into amyloid fibrillar strands. For such molecules in a biologically realistic environment, X-ray diffraction is not applicable and the magnetic resonance of nuclear and electron spins can be leveraged to determine structural detail. In particular, the site-specific signals of nuclear spins can reveal sub-angstrom level structural detail of proteins and molecules. Due to the excellent resolution of NMR spectra, NMR has evolved as the preferred spectroscopic approach for the solution of problems in many areas of science, including physics, chemistry, biology, materials science, and more recently, medicine. Nevertheless, the sensitivity of NMR experiments is low when compared to other spectroscopic approaches. Furthermore, since both high resolution solid and solution state NMR are utilized with increasing frequency in structural studies of macromolecular biological systems-proteins, nucleic acids, etc.-sensitivity continues to be an issue of paramount importance in the successful application of the technique.

DNP has successfully improved the sensitivity in NMR experiments by factors of 20–400 (corresponding to 400–160 000 in acquisition time) [22], [23], depending on the experimental conditions such as temperature, solvent composition, deuteration levels, radical type and concentration, etc. The increased signal intensity shortens the acquisition time, reduces the amount of sample required and allows the acquisition of multidimensional spectra with high signal-to-noise (*S/N*). The following subsections illustrate the mechanism of polarization transfer for efficient DNP at high fields and show that large DNP polarization enhancements are consistently obtained at high field. These results demonstrate applications to structural studies of biologically significant systems which would not be feasible without DNP.

A. Mechanisms of DNP

DNP was first proposed and performed in the 1950's [2], [3], and in the 1980's DNP experiments were incorporated into MAS experiments with the goal of increasing signal intensities in the spectra [6], [7]. MAS of samples in solid-state NMR (SSNMR) spectroscopy reduces line broadening in spectra by spinning at the magic angle of 54.7 deg with respect to the magnetic field, B_0. These initial MAS DNP experiments used 40 GHz microwaves (1.5 T) and the solid effect (SE); signal enhancements of 25 were observed at ~300 K [5], [24]–[27]. Subsequently, DNP experiments were initiated at MIT at 140 and 250 GHz (5 and 9 T fields) [13], [14], [28]–[32] using gyrotrons.

The two mechanisms that are most important for continuous wave (CW) DNP processes in MAS experiments are the solid effect (SE) and the cross effect (CE). Which of the two mechanisms dominate (SE or CE) depends on the size of the inhomogeneous breadth, Δ, and

the homogeneous breadth, δ, of the electron paramagnetic resonance (EPR) spectrum compared to the nuclear Larmor frequency, ω_{0I}.

The SE is a two spin process (Fig. 1(a) left) that governs the polarization process when $\omega_{0I} > \Delta, \delta$ and thus requires a radical with a narrow line such as trityl (Fig. 1(b), (d) left). The frequency dependence of the enhancement profile for trityl is illustrated in Fig. 1(c) (left) and shows minima and maxima when the irradiation frequency is $\omega_{0S} \pm \omega_{0I}$, where forbidden electron-nuclear flip-flops are excited leading to a negative or positive enhancement. Since the SE utilizes forbidden transitions the enhancements scale as ω_0^{-2} and are, therefore, attenuated at higher fields [33].

The CE, a three-spin effect (Fig. 1(a), right), is a DNP mechanism that has been shown to yield more efficient transfers at high-field. It relies on the fact that the resonance frequencies of two electrons, ω_{0S1} and ω_{0S2} in the EPR spectrum, satisfy the condition $\omega_{0S1} - \omega_{0S2} = \omega_{0I}$ (Fig. 1(b), (c) right) and as such the enhancements scale as ω_0^{-1}. Furthermore, the CE works well with a large set of radicals such as nitroxides (TEMPO and its relatives), in which $\Delta > \omega_{0I} > \delta$ at high field. Assuming dipole-dipole couplings exist amongst the two electrons and the nucleus, THz irradiation near either ω_{0S1} or ω_{0S2} flips one of the electrons up, and then there is a subsequent three spin cross relaxation process with the energy difference between the two electron spins going into polarizing the nuclear spin.

The efficiency of CE depends on two spatial factors: (1) the distance between the electron spins, which determines the electron-electron dipolar coupling and (2) the relative orientation of the two radicals, which determines, via the g-anisotropy tensors, the frequency separation $\omega_{0S1} - \omega_{0S2}$. For the case of biradical polarizing agents, both of these factors can be optimized by design of the molecular linkage tethering two nitroxide groups such as that found in 1-(TEMPO-4-oxy)-3-(TEMPO-4-amino)propan-2-ol (TOTAPOL) [35] (Fig. 1(d), right) and bis-TEMPO-bis-ketal (bTbK) [22]. The magnitude of the maximum enhancement obtained with the water-soluble TOTAPOL radical is ~175 at 212 MHz with 6 W of THz power [35], an improvement by a factor of ~4 from monomeric nitroxides like TEMPO. Since the tether connecting the two TEMPO groups is relatively flexible, their relative orientation is not tightly constrained, and many biradicals do not have the correct geometry corresponding to the desired separation frequency. Therefore, with a more rigid tether that can lock the two TEMPOs at a desired relative orientation, it is possible to further improve the performance of a polarizing agent. Enhancements of 250 with 4 W of THz power are achieved using bTbK, a new biradical connecting two TEMPOs with a rigid bis-ketal tether [22]. Thus, significant gains in enhancements have been realized by optimization of polarizing agents for high-field DNP.

An important point illustrated in Fig. 1(c) is that the magnetic field (B_0) has to be swept to the appropriate point in the EPR spectrum in order to optimize the DNP enhancement. In present day DNP spectrometers, this is accomplished with a superconducting sweep coil that was installed on the magnet at the time it was manufactured. In NMR magnets that lack a sweep coil, a tunable source of THz radiation would be useful; see discussion in Section III-F.

Other spectroscopic techniques are enabled by double resonance (NMR and microwave) methods. The Overhauser effect (OE) [2] is important for conducting solids (metals, etc.) and solution samples. Thermal mixing involves a homogeneously broadened EPR spectrum [36] that is present at low magnetic field and as such, is not applicable for THz DNP.

B. Applications of THz DNP in Solids

DNP has been demonstrated to be an extremely versatile technique, resulting in drastic gains in sensitivity in a wide range of biological systems ranging from nanocrystalline peptides [37] and amyloid fibrils [38], to proteins in virus capsids [39], soluble proteins [30], and membrane proteins embedded in lipid bilayers [30]. Similar DNP strategies have recently been extended to materials research and inorganic chemistry applications to enhance signals from nuclear spins on surfaces [40]. This section describes in more detail some of these initial applications of THz DNP.

1) Amyloid Fibrils and Nanocrystals—Proteins are chains of amino acids strung together through covalent peptide linkages. After synthesis, they must fold into the correct three-dimensional structure to perform their biological function. Proteins that mis-fold can aggregate and cause numerous diseases such as Alzheimer's [41], [42]. DNP NMR is well suited to determine the atomic resolution structure of these pathogenic aggregates [43], sometimes referred to as amyloid fibrils or prions. Understanding the structure can yield insight into how and why they form and in turn, help combat the associated diseases.

$GNNQQNY_{7–13}$ (where each letter stands for a single peptide) is a polypeptide originating from the yeast prion protein Sup35p that can form either nanocrystals or amyloid fibrils. At 212 MHz ^{1}H frequency and 90 K, 0.140 THz DNP yields a substantial enhancement factor of 120 on nanocrystals of GNNQQNY, permitting the acquisition of 2D spectra in only 20 minutes due to the excellent sensitivity available with DNP [37]. The biradical polarizing agent, TOTAPOL, is too large to penetrate into the nanocrystals, yet leads to ^{13}C and ^{15}N spectra with enhancements of 120 for the peptide resonances and 160 for the solvent, illustrating that ^{1}H spin diffusion effectively distributes the enhanced polarization throughout the lattice. These initial experiments have been extended to higher fields in a study using a 263 GHz commercial Bruker spectrometer [20] which demonstrated an enhancement of 20 on nanocrystals [Fig. 2(a)] and 35 on amyloid fibrils of GNNQQNY [Fig. 2(b)]. This drastic gain in sensitivity may be used for structural determinations of GNNQQNY and other fibrils.

2) Membrane Proteins—Bacteriorhodopsin (bR) is a membrane protein which functions as a light-activated H^+ pump. A retinal chromophore in the center of the protein that is at equilibrium between two conformations [Fig. 3(b)] absorbs a photon of light that initiates a photocycle consisting of distinct intermediates [Fig. 3(a)]. Despite the fact that there are now ~70 crystal structures available for this protein, the mechanism for its function as a pump is not yet established. The X-ray structures have thus far been unable to resolve essential structural details such as torsion angles in the retinal chromophore in the photocycle intermediates [48] and to discriminate if the protein is an H^+ pump (as assumed for 30 years) or a backward directed OH^- pump.

SSNMR structural methods are capable of measuring torsion angles and internuclear distances with high precision, but the relative insensitivity of traditional SSNMR is a severe limitation with large proteins. Recording a single 2D data set on a protein with a large effective molecular weight of 32 kiloDaltons typically requires 10 days of signal averaging. However, with DNP enhancements even as low as $\varepsilon = 20$, it can be done in less than an hour. This in turn permits the measurement of a variety of torsion angles and distances in the resting state and in photointermediates that will elucidate the pumping mechanism of this protein. Accordingly, experiments confirm that DNP is capable of enhancing the NMR signals in the active site deeply buried in bR by a factor of 40 [49]. Fig. 3(c), (d) shows 2D correlation spectra of a sample which has specific labels at the C14 and C_ε position in the active site [yellow box of Fig. 3(b)]. With THz DNP, in only 7 hours, it is possible to record

a spectrum showing correlation peaks between the C14 and C_ε carbons [45]. With the sensitivity boost from THz DNP, it was possible to record multiple correlation spectra in which the polarization transfer time between the two carbon sites was varied. The dipolar coupling strength, which is directly related to the distance between the two spins, can then be extracted by the build-up profiles of the correlation peak intensity [Fig. 3(d)]. In addition to these experiments that measured inter-nuclear distances to sub-angstrom precision, THz DNP also revealed heterogeneity in the different conformational states of bacteriorhodopsin [47].

In the resting state of the protein, what was previously thought to be only one conformer, bR_{555} clearly is resolved as two resonances in the 2D spectrum (Fig. 3(e), left). Furthermore, the L intermediate [blue box of Fig. 3(a)] was shown to actually consist of four states (Fig. 3(e), right), three of which are shunt states that do not result in a proton being pumped across the membrane [47].

C. DNP for Solution State NMR

There is considerable interest in applying DNP techniques to high field solution NMR experiments. Recently, significant progress has been made in performing DNP directly in the solution state using a 263 GHz gyrotron [17]. However, it is also possible to perform a polarization step and melting *in situ*, the latter being performed with CO_2 laser radiation. This experiment is referred to as *in situ* temperature jump DNP (TJ-DNP) [23].

A schematic representation of the TJ-DNP cycle is shown in Fig. 4. For this experiment, the DNP NMR probe is maintained at 90 K, and the frozen sample is polarized with microwave irradiation at 140 GHz. Polarization is then transferred by cross polarization from ^1H to ^{13}C. The sample is then rapidly melted by a CO_2 laser pulse (10 W for 1.2 s, $\lambda = 10.6$ μm), and a ^{13}C solution NMR signal is immediately recorded with ^1H decoupling. Fig. 4(b) shows the solution spectrum (right) as well as the SSNMR ^{13}C spectrum obtained with DNP but without melting. For this sample (^{13}C-urea in DMSO/water), the sensitivity enhancement that is observed is 400 ± 15 relative to the normal solution NMR experiment carried out entirely at room temperature [23]. Fig. 4 shows a spectrum in which TJ-DNP is integrated into a 2D ^{13}C-^{13}C experiment.

III. Gyrotrons for DNP NMR

A. THz Sources

As DNP NMR experiments move to higher magnetic fields, several requirements make gyrotrons the most practical source for THz radiation. As seen in Table I, the THz source should ideally produce a minimum of 20 W CW. When coupled with typical transmission line efficiencies of 50 to 80% from the source to the sample, the available power at the sample will be sufficient for saturation of the enhancement in most cases. It is highly desirable to have the output beam in a nearly Gaussian free space mode capable of direct injection and matching into the wave-guide transmission line. For a Gaussian beam, the ideal waist size is equal to about 0.64 of the waveguide radius of the transmission line. Table I also lists the frequency and power stability needed for the duration of the NMR signal acquisition period (≥36 hours). Additionally, the lifetime of the device must also be considered, due to the major capital and personnel investments involved in NMR research.

The generation of millimeter, sub-millimeter and THz radiation at high power has proved to be a significant challenge. In Fig. 5, updated from the review article [50], the state-of-the-art capabilities for solid state and vacuum electron sources are shown. As seen in Fig. 5, solid state devices in the THz range suffer from scalability and efficiency issues that lead to limited output powers. However, they have proved useful in some DNP NMR experiments

that use small sample sizes and metallic resonators [6], [51]–[53] suitable for aqueous and static (non-MAS) DNP experiments. These experiments have relied on sample volumes that occupy a small fraction of the resonator. However, to optimize S/N in MAS DNP experiments, large sample volumes are required. Furthermore, metallic resonators or rotating metallic components are not permissible in the stator as they would produce eddy currents and levitation effects.

Classical microwave tubes, e.g., klystrons and traveling-wave tubes, can produce high power (hundreds of watts) electromagnetic radiation up to 100 GHz, but these slow wave devices require physical structures in the interaction cavity that are much smaller than the wavelength of operation. This small element size produces difficulties with thermal damage and manufacturing of the interaction cavity when the frequency is extended into the THz range. Furthermore, at THz frequencies, slow wave devices suffer from reduced lifetime due to electron beam interception and high heat loads. The Extended Interaction Klystron (EIK) is a possible source for THz radiation needed in DNP experiments. As an oscillator, it has achieved an average output power of 7 W at 220 GHz and 0.3 W at 280 GHz [54], [55]. The EIK is promising for DNP applications, but has limited power and may have limited lifetime at THz frequencies.

Electron cyclotron resonance masers (gyrotrons) are capable of producing high average power in the microwave, millimeter wave and THz bands [56]. Due to the overmoded cavities used in gyrotrons, they remain the only demonstrated, highly stable device capable of producing adequate power levels (a minimum of 10 W CW) with an adequate lifetime (about 100 000 hours) in the frequency range of interest for DNP NMR.

B. Fundamentals of Gyrotrons

In gyrotrons, the emission of coherent THz radiation results from the resonant interaction between the eigenmodes of a cavity, typically cylindrical, and a mildly relativistic electron beam that is gyrating in a constant axial magnetic field. The basic configuration of a gyrotron, Fig. 6, consists of a magnetron injection gun (MIG) that launches an annular electron beam into the hollow bore of a solenoidal magnet. The magnetron injection gun is located at the bottom of Fig. 6. The axial magnetic field is produced by a DC superconducting magnet. A second magnet can be added at the location of the MIG to provide additional control of the electron beam compression and velocity ratio. In the MIG, the orientation of the DC electric field that extracts the electron beam from the cathode produces a beam that has both a perpendicular and parallel velocity component with respect to the axial field produced by the solenoidal magnet. As the electron beam travels into the central bore, it undergoes adiabatic compression that increases its orbital momentum. The electrons enter a metallic cavity that has an eigenmode resonance that is close in frequency to a harmonic of the gyration frequency of the electron. The electron beam surrenders some of its kinetic energy to the electromagnetic mode through stimulated emission. The electrons exit the cavity and are deposited on a metallic collector. The gyrotron resonator supports a high order cavity mode that is difficult to transport over long distances. It is often convenient to convert the mode into a Gaussian beam that can be efficiently extracted in a transverse direction using mirrors.

In order for the electron beam to interact with the electromagnetic mode in the cavity, a harmonic of the relativistic electron cyclotron frequency must be close to the frequency of oscillation for the cavity mode [57]. The relativistic cyclotron frequency is

$$\Omega_c = eB_0/\gamma m_e \quad (1)$$

where e is the charge of the electron, B_0 is the DC axial magnetic field, m_e is the electron mass and γ is the Lorentz factor $(1 - \upsilon^2/c^2)^{-1/2}$, where υ is the velocity of the electron and c the speed of light. In a cylindrical cavity, of radius r_w and length L, the dispersion relation for TE modes is

$$k^2 - k_\perp^2 - k_z^2 = 0 \quad (2)$$

where $k = \omega/c$ is the wave vector in free space, ω is the frequency of the THz wave, $k_\perp = \nu_{mn}/r_w$ is the transverse propagation constant, ν_{mn} is a root of the Bessel function $J'_m(x)$ and k_z is the axial propagation constant (approximately $q\pi/L$, where q is an integer). The cyclotron beam mode dispersion relation or Doppler shifted resonance condition is

$$\omega - k_z \upsilon_z - s\Omega_c = 0 \quad (3)$$

where υ_z is the axial velocity of the electrons and s is the integer cyclotron harmonic number. When these dispersion relations are equally satisfied, as seen in Fig. 7, oscillation and stimulated emission can occur. The dotted/dashed line and the dashed line in Fig. 7 are the cyclotron beam mode dispersion relation for and s = 1 and s = 2, respectively. The black circle is a fundamental forward wave oscillation, the square is a second harmonic forward wave oscillation and the diamond is a fundamental backward wave (BW) oscillation. Traditionally, gyrotrons interact with the fundamental forward wave [13], [14], [20]; however, the second harmonic forward wave is useful for higher frequency experiments [15], [16], [58], [59] and the BW interaction is used at the first or second harmonic to provide the frequency tunability in gyrotrons for DNP NMR experiments.

The cavity in a gyrotron typically consists of a central cylindrical region with a downtaper on the gun side and an uptaper on the collector side. A cross section of the cavity is shown in Fig. 8. Superimposed over the cavity is the axial electric field profile for the mode of the cavity shown, which is a $TE_{4,3,1}$ mode. The interaction between the electron beam and the cavity mode occurs only at the radius of the annular electron beam, r_e, as shown in the insert of Fig. 8. Because the cavity modes are non-uniform in the radial direction, the strength of the interaction between the beam and a cavity mode is determined by the radial placement of the electron beam. This can be advantageous (especially in second harmonic experiments) by allowing for the selection of a desired mode.

C. Nonlinear Theory of Gyrotrons

For an exact understanding of the operation of a gyrotron oscillator, the interaction between an energetic electron and the electromagnetic mode confined in the interaction cavity (resonator) must be described. In a gyrotron, kinetic energy is extracted from the electron beam as it passes through the interaction cavity. However, a gyrotron does not extract any energy from the axial component of the velocity, only from the transverse component. This energy extraction is made possible because an electron traveling in a circular path orthogonal to a DC magnetic field will feel an accelerating or decelerating force from the resonant oscillating electric field that can deposit or extract energy from the electron. The initial applied force from the cavity mode results in some electrons gaining energy and some electrons losing energy. The more energetic electrons rotate slower and the less energetic electrons rotate faster, because of the dependence of γ and Ω_c on velocity and energy. The different rotational frequencies produce phase bunched electrons that act coherently to deposit energy into the electromagnetic mode of the cavity. This process can be described by the pendulum equations that relate the change in energy and momentum for the electron to the electric and magnetic fields that are present. The equations of motion for the electron are

$$\frac{\partial \varepsilon}{\partial t} = -e\mathbf{v} \cdot \mathbf{E} \quad (4)$$

$$\frac{\partial p}{\partial t} = -e(\mathbf{E} + \mathbf{v} \times \mathbf{B}) \quad (5)$$

where the electron energy is ε, the momentum *p*, the THz electric field is **E**, the DC magnetic field is **B** and the velocity of the electron is **v**. The instantaneous kinetic energy and momentum of a relativistic electron are and $\varepsilon = \gamma m_e c^2$, and $|p| = \gamma\beta m_e c$, respectively, where $\gamma = (1 - \beta_\perp^2 - \beta_z^2)^{-1/2}$ and $\beta = \upsilon/c$.

It is useful to convert these equations into normalized variables for the practical case of a cylindrical resonator by taking into account the strength of the coupling between the electron and electromagnetic mode. The conversion to the normalized pendulum equations is covered in detail by [57], [61] and results in

$$\frac{\partial u}{\partial \zeta} = 2Ff(\zeta)(1-u)^{n/2}\sin\theta, \quad (6)$$

$$\frac{\partial \theta}{\partial \zeta} = \Delta - u - nFf(\zeta)(1-u)^{(n/2-1)}\cos\theta. \quad (7)$$

where the normalized variables are the electron energy *u*, the electron phase θ, the axial position ζ, the field strength *F* and the magnetic field detuning Δ. With a cavity length *L*, the normalized cavity length μ and assuming a Gaussian axial field profile with

$$\mu \equiv \pi \frac{\beta_\perp^2}{\beta_z^2} \frac{L}{\lambda} \quad (8)$$

$$f(\zeta) = e^{-(2\zeta/\mu)^2}. \quad (9)$$

The beam-wave coupling has been incorporated into *F* [61]. These coupled differential nonlinear equations of motion describe a gyrating electron interacting with an electromagnetic field by tracking the normalized transfer of energy and the phase of the electron. Equations (6) and (7) are only functions of three parameters: *F*, μ and Δ. In a gyrotron an electronic efficiency of up to 70% is achievable with the optimization of these parameters [61].

D. Development of THz Gyrotrons

The discovery of the cyclotron resonance instability by Twiss [62], Schneider [63], and Gapanov [64] was followed by the first detailed experimental demonstration by Hirshfield and Wachtel [65]. The first high power gyrotron in the THz band produced a kilowatt of power at a frequency near 300 GHz [66]. Pulsed THz gyrotron oscillators with several hundred kilowatts of power were also developed [67]–[69], reaching almost 1 MW of power at 300 GHz [70]. In the past two decades, progress has been made on providing useful millimeter and sub-millimeter wave sources for electron cyclotron resonance heating (ECRH) of plasmas [71], [72].

At very low power levels, step tunable gyrotrons have been demonstrated at frequencies in the THz band for spectroscopy [73]–[75]. Gyrotrons were developed at power levels of 10–100 W for application to DNP NMR and EPR experiments [13]–[16], [20], [58], [59]. The gyrotrons for DNP NMR must meet exacting specifications for reliability, efficient power conversion, frequency bandwidth and signal stability, as listed in Table I. With interest in developing this technology for higher frequency NMR experiments, these THz sources present a challenge to THz technology for sources, transmission lines and related components. A comprehensive review of the history and present state of THz vacuum electronics is provided in this journal issue [76].

E. DNP Experiments With Gyrotrons

In 1992, the first use of a gyrotron for a DNP NMR experiment was reported by Becerra *et al.* [13] using a 140 GHz CW gyrotron capable of producing 20 W. Signal enhancements for polystyrene doped with BDPA of 10 for ^{1}H and 40 for ^{13}C were reported when comparing NMR spectra recorded with and without microwave power. The 140 GHz gyrotron operated in the $TE_{0,3,1}$ mode of a cylindrical resonator with a 42 kV, 10–100 mA electron beam producing 20 W CW and 200 W pulsed. This was the first gyrotron with enough stability for phase-coherent magnetic-resonance spectroscopy. The power is converted internally to the TE_{01} mode and extracted from the gyrotron after a miter bend through a window. A transmission line and mode converters provide the power to a WR-8 waveguide that goes to the sample and radiates the power along the axis of rotation of the MAS sample. Recently, the gyrotron was upgraded to be operated with a lower voltage MIG [29], [77] with the key parameters of the 140 GHz gyrotron listed in Table II. The bandwidth of the gyrotron has been measured using a heterodyne receiver system. The emission bandwidth of the gyrotron was found to be 1 MHz at 60 dB below the carrier [78], [79]. This is the most sensitive measurement to date of noise in a gyrotron, and the results assure that parasitic modes do not participate in the excitation of the electron spins in DNP NMR spectroscopy. This gyrotron has remained in service for nearly two decades of operation.

A 250 GHz DNP NMR system [14], [80] was commissioned at MIT in 2000 with a design that improved upon the 140 GHz spectrometer. This gyrotron produces 15 W with a 12 kV, 35 mA electron beam in the $TE_{0,3,2}$ mode. ^{1}H Enhancements of up to 170 have been observed for 1-^{13}C-glycine at temperatures of 20 K using a MAS probe [14]. The gyrotron, transmission line and NMR setup are shown in Fig. 9. The 250 GHz gyrotron is designed to operate in a vertical orientation in order to simplify support and alignment. A radial bore in the magnet allows the transmission of the microwave power through a side vacuum window of the tube. As a result, the electron beam and microwave power can be separated just after the interaction in the gyrotron cavity. An internal Gaussian beam mode converter was included in the design. This reduces ohmic losses in the output waveguide and simplifies the design of the beam collector and microwave transmission line. A specially built corrugated transmission line with very low loss brings the power from the gyrotron to the sample [81]. The transmitted beam had a measured Gaussian beam content of 93% [82]. The gyrotron output power is monitored and controlled by feedback stabilization.

In recent years, gyrotrons have been built for DNP NMR research by several groups throughout the world. The first commercial DNP system using a gyrotron is a 263 GHz/400 MHz NMR spectrometer that was developed in 2009 by Bruker BioSpin [20], shown in Figs. 10 and 11.

More recently, gyrotrons that operate at the second harmonic of the electron cyclotron frequency ($\omega \approx 2\Omega_c$ have been developed for DNP NMR experiments due to the reduced requirements placed on the magnetic field of the gyrotron (half the magnetic field required for fundamental operation). Unique physics and engineering challenges arise at the second

harmonic due to reduced efficiency and fundamental mode competition. These difficulties were overcome by careful design of the resonator and choice of the operating mode which is relatively isolated in the mode spectrum. The first completed second harmonic gyrotron for DNP NMR applications was a 10 W, 460 GHz gyrotron oscillator for NMR at 700 MHz [15], [16], [78], [83]. The electron beam parameters during operation are a voltage of 12 kV, current of 140 mA, with a beam radius of 1.03 mm. The gyrotron is shown in Fig. 12.

With the completion of two additional second harmonic sources in 2009 [58], [59], the first DNP enhancements using second harmonic gyrotrons were reported in 2010 at 260 GHz [17] and 395 GHz [19]. The 260 GHz experiment, shown in Fig. 13, utilized a 20 W gyrotron and was able to produce signal enhancements of −79 on an aqueous solution of Fremy's salt [84], far exceeding previous results using a solid state source [17], [53]. The 395 GHz gyrotron is capable of producing 40 W using the TE_{06} mode of a cylindrical cavity with an enhancement of 10 for 1 M $^{13}C_6$-glucose and 10 mM TOTAPOL [19]. A second harmonic gyrotron for DNP has also been built at 330 GHz [16].

F. Tunability

Due to the extremely sensitive frequency requirements of DNP, either a NMR magnet equipped with sweep coils or a THz source that is continuously tunable can be very valuable. Fabricating a gyrotron cavity to operate at a predetermined frequency with $\Delta f_{set} \approx$ 50 MHz accuracy would be a major engineering requirement due to the extremely tight tolerance placed on the cavity radius, as can be seen from (2). It is also difficult and expensive to alter the magnetic field of the NMR experiment to match the gyrotron with such accuracy. With a tunable source that is able to vary the frequency over a range much greater than Δf_{set} this engineering challenge is alleviated. The frequency of the THz radiation must match the absorption condition for the appropriate DNP mechanism in order to provide a signal enhancement. If the frequency is not correct, a drastic change in enhancement will be observed, as seen in Fig. 1(c). Furthermore, sweeping the frequency over the entire range of the EPR spectrum is of interest to the user. In general, the width of the EPR spectrum grows linearly with the magnetic field of the NMR experiment adding an additional challenge to higher frequency (typically second harmonic) sources. Continuous tunability in gyrotrons with TE_{mnq} cavity modes can be achieved by keeping the transverse mode numbers (m, n) constant and varying the axial mode number (q). By keeping the transverse index the same, nearly continuous tuning can be achieved by either voltage or magnetic field tuning without affecting the mode converter and transmission line performance. Tuning is improved by increasing the cavity length resulting in a decreased frequency shift from adjacent axial modes via their hybridization. Continuous tunability in a gyrotron for DNP was first reported by Hornstein *et al.* [15]. In this gyrotron the increased cavity length to lower the oscillation start current for the desired second harmonic mode, led to the hybridization of axial modes, with 2 GHz of tuning reported for fundamental modes near 230 GHz and 50 MHz for the second harmonic mode at 460 GHz, as seen in Fig. 14. When the 460 GHz gyrotron was later rebuilt to operate in the $TE_{11,2}$ mode, over 700 MHz of tuning was observed at the second harmonic [16].

This technique for achieving continuous tuning has also been implemented in a 330 GHz second harmonic oscillator [60]. A continuous tuning range of 1.2 GHz was observed experimentally via a combination of magnetic, voltage and thermal tuning. Thermal tuning is achieved by the precise control of the cavity cooling, allowing the cavity to expand or contract as needed. An additional advantage to long cavities is that the start current for oscillations is lowered for all axial modes allowing for operation with smaller beam powers. For a beam voltage of 10.1 kV the oscillation start current for the 330 GHz gyrotron is shown in Fig. 15.

Tuning of over 1 GHz has recently been achieved in a 395 GHz gyrotron [59], [85]. The 1.6 GHz of tuning, shown in Fig. 16, demonstrates how switching axial mode numbers allows for nearly continuous tuning with magnetic field even with fundamental mode experiments at very high frequencies. On the left side of Fig. 16, the gyrotron is interacting with a forward wave and on the right side of the figure a backward wave.

G. Internal Mode Converters

Extracting THz radiation efficiently from gyrotrons in a manner useful for DNP NMR spectroscopy is very challenging. Internal mode converters that provide high quality Gaussian beams provide the most utility due to the attractive qualities that Gaussian beams provide with respect to transmission, as discussed in Section IV. Internal mode converters are a topic of great interest in the gyrotron community at large due to their power extraction efficiency. Internal mode converters in the form of step cut launchers for azimuthally symmetric modes and helical cut launchers for rotating modes were pioneered by Vlasov [87], [88]. Modern mode converters include the use of quasi-parabolic mirrors to correct for the ellipticity of the beam produced by the launcher. Designs are also optimized using numerical codes, such as the electric field integral equation code Surf3d [89]. Examples of internal mode converters are shown in Fig. 6, labeled as item 6, and in Fig. 17(a). This mode converter was designed for use with a $TE_{11,2}$ mode at 460 GHz [90] with a helical cut launcher, parabolic mirror and two flat mirrors shown in Fig. 17(a). The profile of the gyrotron output beam measured with a Spiricon Pyrocam III pyroelectric camera is shown in Fig. 17(b). The resulting beam is 92% Gaussian with a waist of $w_x = 4.1$ mm and $w_y = 4.6$ mm. Similar mode converters have now been implemented on most DNP gyrotrons [14]–[16], [20], [58].

IV. Transmission Lines

The power generated by the THz source (gyrotron) must be transmitted to the sample with low loss. In the THz band, it is not possible to use conventional single mode rectangular waveguide for transmission, since the ohmic loss in such guides is much too large. The location of the source, typically a few meters from the NMR spectrometer, requires that the loss per meter be kept as low as possible. Transmission lines for terahertz radiation are an area of intensive research at the present time. Since the frequency bandwidth needed for DNP NMR systems is usually very small, the transmission line can be optimized for a single frequency, thus simplifying the problem significantly. The number of approaches to the design of the transmission line is quite extensive. Free space beaming techniques rely on propagation of a Gaussian-like beam via a series of mirrors and/or lenses. This approach has low loss but may have issues of safety and the stability of alignment. The most common approach is the use of overmoded waveguides, in which the guide radius is much larger than the wavelength. Such waveguides can be corrugated metallic waveguides, dielectric waveguides or dielectric lined metallic waveguides. Reviews of the properties of overmoded waveguides are given by Bhartia and Bahl [91] and Thumm and Kasparek [92].

Fig. 18(a) shows a schematic of a corrugated metallic waveguide. The guide has grooves of depth d that are one quarter wavelength. The radius a is much larger than a wavelength. The corrugations are optimized when the groove depth $d \approx \gamma/4$, period $w_1 \approx \gamma/3$ and tooth width $w_2 < w_1/2$. Fig. 18(b) shows the transmission line used in the MIT 250 GHz DNP NMR system [81]. Fig. 18(b) illustrates some of the key features of a low loss transmission line. The main transmission line is a 22 mm diameter ($a = 11$ mm) metallic corrugated waveguide made of aluminum. The corrugations d are one quarter wavelength in depth (0.3 mm), one quarter wavelength wide ($w_2 = 0.3$ mm), with a period of $w_1 = 0.4$ mm. Two 0.254 m waveguide sections, fifteen 0.124 m waveguide sections and one 0.064 m directional coupler block were assembled with outer diameter clamps to achieve the desired waveguide length.

The modes and ohmic loss in a corrugated waveguide have been developed using the theory of Doane [93]. The linearly polarized output of the gyrotron excites a linearly polarized mode (or modes) in the waveguide [94]. The lowest order mode is the hybrid mode HE_{11}, whose transverse electric field is given by:

$$E^{\perp}(r,\phi)=(X_{01}/a)J_0(X_{01}r/a) \quad (10)$$

where X_{01} is 2.405 and J_0 is the zeroth-order Bessel function. This expression is valid when the corrugation depth is approximately one quarter wavelength and the radius a is much larger than the wavelength.

The estimated ohmic loss in the overmoded waveguide of Fig. 18(b) is less than 10^{-3} dB/m and is thus negligible. The measured loss for the 22 mm diameter waveguide portion of the transmission line of Fig. 18(b) is shown as open circles in Fig. 19 and amounts to less than 1% per meter.

For perfect excitation of the HE_{11} mode on the transmission line, the overall transmission line loss is expected to be dominated by loss at miter bends and by tilts and offsets in the fabrication and alignment of the waveguide components. In practice, however, the loss may be dominated by the imperfections in the THz beam entering the transmission line and poor coupling of the beam to the line. When the output beam of the gyrotron is not a perfect Gaussian beam or the output beam is not perfectly matched (due to tilts and offsets) upon insertion into the waveguide, high losses may be found on the transmission line [95].

The transmission line shown in Fig. 18(b) has directional couplers for measuring forward and reverse power. They have been fabricated by stretching metal wires across the waveguide surface area and have only a 2.6% insertion loss, as shown in Fig. 19. This approach was found to be superior to using a quartz coupler. A smaller diameter waveguide in the probe is necessitated by the limited space in the probe, this transition can be performed with waveguide tapers or mirrors. Bends in the transmission line may be accomplished using a right angle bend, called a miter bend, in the waveguide or using a mirror box. The transmission line of Fig. 18(b) has only one right angle bend, and it is accomplished using two mirrors. The mirrors also match the beam from the 22 mm waveguide into the 8 mm waveguide used in the NMR probe. Due to losses induced by imperfections in the Gaussian beam quality of the gyrotron and by errors in the alignment of the components of the transmission line, the transmission efficiency from the gyrotron output window to the sample is typically in the 50%–80% range [81], [82].

The transmission line shown in Fig. 18(b) is only one example of successful transmission lines used in DNP NMR research. Recently, a very long transmission line using corrugated waveguides and switches has been successfully implemented on a 260 GHz gyrotron system for DNP NMR [96], [97]. A fully optical (mirror) transmission line using a mirror relay line has also recently been implemented for a DNP NMR spectrometer system [98]. Future research will concentrate on making these transmission lines simpler and more efficient.

V. Versatile Probes for DNP

MAS DNP probes can couple frequencies spanning eight orders of magnitude of the electromagnetic spectrum to samples under study. The DNP probe for experiments at a 9 T magnetic field shown in Fig. 20 integrates an RF circuit that resonates an inductor surrounding the sample at 38, 96, and 380 MHz to control and detect ^{15}N, ^{13}C, and ^{1}H spins, respectively. 250 GHz and 532 nm radiation channels illuminate the sample to excite the EPR and visible spectra [45]. Additionally, probes also house a pneumatic spinning module to mechanically rotate the sample at frequencies up to 8 kHz at an angle of 54.7° (the Magic

Angle) with respect to the B_0 NMR field. This motion partially averages anisotropic chemical shift and dipolar tensors that would otherwise result in broad NMR line shapes and poorly resolved spectra.

A. Cryogenic Magic Angle Spinning

Electron spin relaxation times, T_{1S}, in MAS DNP experiments increase at lower temperatures. Electron spins relaxing faster than the rate of transfer of polarization to the nuclear spins result in inefficient DNP transfers. Utilizing polarization agents with long (T_{1S} ~ 1 ms) longitudinal relaxation at ambient temperatures [5] is a strategy to circumvent this issue, and these T_{1S}'s are generally observed in radicals such as trityl with narrow powder patterns. However, these systems lead to a SE mechanism that does not scale well at higher magnetic fields. A more general strategy is to dope the sample with radicals that have a larger g-anisotropy that supports the CE mechanism and to perform the experiments at low temperatures (~90 K), where the relaxation times of both the electron and nuclear spins are longer. After the initial electron to nuclear polarization step, inherent proton spin-lattice relaxation mechanisms compete with the microwave driven polarization of the nuclear spins. The DNP enhancement thus has a strong dependence on temperature, ranging from <5 at 160 K [20], 100 at 85 K [45], and 170 at 20 K [14] for model samples frozen in a glassy matrix and at magnetic fields of 9–9.5 T.

Achieving a uniform cryogenic sample temperature without exposing sensitive elements in the probe to a harsh environment is accomplished by thermally isolating the sample chamber and using the bearing and turbine gases needed for MAS spinning also as variable temperature cryogens [45]. A vacuum jacketed dewar [Fig. 20(b)] and the use of insulating material in the probe body reduces heat transfer from the sample chamber to the probe box and magnet bore which are maintained at ambient temperature.

In MAS DNP experiments, cooling to near 80 K can be achieved through a heat exchange process with liquid nitrogen. Since the DNP enhancement is extremely sensitive to temperature in the range of 80 K, the temperature typically must be regulated to within 0.5 K. Furthermore, the generation and trapping of photointermediates in photoactive proteins such as bR requires temperature control over a wide temperature range from 90 to 273 K [100].

B. Cryogenic Sample Exchange

Due to the complicated nature of overmoded transmission lines, as discussed in Section IV, misalignment during sample exchange can result in excessive down time and reduced performance. In addition, the magic angle and shim coils become misadjusted when the probe is physically moved out and back into the magnet, which can lead to degradation of spectral resolution [Fig. 20(c)]. Sample eject systems operate at low temperatures and avoid physical adjustments to the transmission line, warming and cooling the probe, while at the same time retaining much better experimental stability [45].

C. RF Circuit

RF circuits such as that in Fig. 21 couple power from RF amplifiers and the NMR spectrometer to an inductor surrounding the sample. The RF circuit is used to detect the NMR signals which are ultimately the data that result from an DNP NMR experiment. The resonant frequencies of the RF circuit must match that of the nuclear spins to efficiently utilize the RF power and generate strong fields orthogonal to the main magnetic field of the superconducting NMR magnet. The tuning, matching, and isolation elements in the RF circuits can either be located near the coil or utilize a transmission line to physically separate the elements from the harsh cryogenic environment near the sample [101], [102]. The

severely constrained spacing inside the bore of NMR magnet has led to the use of the THz waveguide as the inner conductor for the RF transmission line which carries the 3 RF frequencies to the RF coil.

D. THz Coupling to Sample

The sensitivity enhancement in DNP experiments depends strongly on the intensity of the millimeter waves in the sample of interest. Specifically, it is important to know the magnitude of the THz field, B_{1S}, that is orthogonal to B_0 and oscillates at the frequencies leading to polarization transfer. The THz beam is brought through the probe in a small diameter waveguide, as shown in Fig. 21. The THz radiation is launched from the end of the corrugated waveguide in a Gaussian power distribution generated from the HE_{11} mode of the corrugated transmission line, as shown in Fig. 18. However, the RF coil, large sample volume, and other physical requirements of the MAS DNP experiment hinder the illumination of the sample with the THz waves, and indeed the implementation of a high Quality factor resonator surrounding the sample.

Other strategies of coupling the THz power axially down the rotor (rather than the perpendicular coupling shown in Fig. 22(b) have been explored by other groups at 39 GHz [5] and 394 GHz [19]. Although successful at lower frequencies, axial coupling at higher frequencies (>200 GHz) is rather inefficient due to the dielectric constant and loss tangent of the sample [82]. Optimization of THz coupling and RF performance is crucial to overall quality of the probe [103].

Recently, high frequency structure simulator (HFSS) was used to calculate how the THz radiation travels from the antenna, diffracts through the coil, and is distributed across the sample, as shown in Fig. 22 [82]. Simulations were performed using a linearly polarized Gaussian beam as the input with a sample dielectric constant extrapolated from measurements at 140 GHz. The sample is dissolved in a water/glycerol mixture and held in a sapphire rotor with a 2.4 mm internal diameter. The sample extends the full length (12.45 mm) of the RF coil. In the sample the calculated average B_{1S} THz field is 13 μT/$W^{1/2}$. The B_{1S} in the sample varies quite drastically from 3 to 50 μT/$W^{1/2}$ due to diffraction effects. In comparison, EPR and ENDOR resonators are able to achieve much higher average B_{1S} values per $W^{1/2}$ and improved homogeneity. Specifically, by using low order metallic resonant structures and sample volumes that occupy a small fraction of the resonator, B_{1S} values on the order of 1 mT/$W^{1/2}$ have been reported [51], [104], [105]. As discussed previously these metallic resonators are not suitable in MAS DNP experiments, but alternate methods for increasing the *Q*-factor of large volume samples could prove beneficial.

The enhancement observed in a DNP CE experiment can be described using the calculated B_{1S} and a simplified expression for the steady state enhancement derived by Wollan [10]. Since the microwave field, $\omega_{1S} = \gamma_S B_{1S}$, is inhomogeneous, as demonstrated in Fig. 22, the expression must be integrated over the field dependence for the sample volume

$$\varepsilon = \frac{1}{V}\varepsilon_{\max}\int \frac{\alpha\omega_{1S}^2}{1+\alpha\omega_{1S}^2}\,dV \quad (11)$$

where $\alpha = (T_{1S}T_{2S})/2$ and T_{1S} and T_{2S} are the electronic longitudinal and transverse relaxation times. The factor of 1/2 converts from the time averaged linearly polarized ω_{1S}^2 to the time averaged circularly polarized component that interacts with the electrons. A quadratic dependence is observed at low ω_{1S}^2 when the magnitude of the product $T_{1S}T_{2S}\omega_{1S}^2 \ll 1$. It then saturates at high ω_{1S}^2. T_{1S} for a Nitroxide radical is expected to range from 10 to 400 μs in the 90 K temperature regime, and T_{2S} is a strong function of radical

concentration being in the range of 10–200 ns for the 20 mM electron concentration in the sample evaluated in Fig. 23. Fig. 23 is a plot of the experimental enhancement of 1 M ^{13}C-urea and 10 mM TOTAPOL dissolved in d_8-glycerol/D_20/H_20 (60/30/10% by volume) [106], [107] vs. input power at 250 GHz for the sample and probe described in Figs. 20 and 21 and the field distribution shown in Fig. 22. Calculating the value of $\gamma_S B_{1S}$ at the level of a mesh element volume defined by the HFSS model is crucial to understanding the DNP enhancement data and, indeed, to modeling the enhancement more generally obtained from the cross effect [10].

VI. Conclusion

Dynamic nuclear polarization has become firmly established as a powerful technique for enhancing signal intensities in NMR spectroscopy. In DNP NMR, the required frequencies for microwave irradiation of the sample have increased as NMR has moved to progressively higher magnetic fields due to the improved resolution and sensitivity. Modern NMR spectrometers are presently operating at proton frequencies close to 1 GHz, corresponding to fields of 23 T. The microwave frequencies needed for these spectrometers enter the terahertz regime as the magnetic field exceeds 10.7 T. Stated another way, for NMR spectrometers operating above 450 MHz, the required microwave frequency for DNP NMR is in the terahertz range.

The gyrotron is capable of achieving the power and stability requirements for THz DNP NMR. The number of gyrotron-based DNP NMR systems was only a single system in 1990 and increased to two systems only in 2000 (both at MIT). However, as pointed out by Griffin and Prisner [9], DNP NMR is now enjoying a “renaissance”. There are now approximately 20 THz DNP NMR systems either operating or under construction [108] and more systems will surely follow. THz DNP NMR will thus be recognized as a major present-day application of THz technology.

The lack of THz sources has led to complex schemes such as dissolution or shuttle DNP [12], [109], [110], where the sample is polarized in a lower magnetic field region and then transported to the high field region for signal acquisition. Low power solid state sources have also been employed in static DNP experiments [6], [51]–[53], [111], [112] that would likely benefit from higher power THz sources [17]. The appeal of resonant structures can be illustrated by looking at an expression for the Quality factor (Q) of the sample region defined as

$$Q=\omega W/P \quad (12)$$

where ω is the resonant frequency, $W = W_e + W_m$ is the energy stored in the cavity, W_e and W_m are the electric and magnetic energy and P is the input power. We can assume that $W_e \sim W_m$ and $W_m \propto \langle B_{1S}^2 \rangle V$, where V is the volume. With these simple substitutions we can rewrite (12) for the quantity of interest in DNP

$$\langle B_{1S}^2 \rangle \propto QP/V \quad (13)$$

Equation (13) shows that in order to minimize the required power P it is advantageous to work with samples of small size (small V) contained in high Q cavities. In NMR experiments, however, it is useful to use larger samples since the NMR signal strength increases with the sample size (or volume, V). In addition, it is not easy in MAS NMR to construct optimized resonators with the highest possible Q. One limitation on the Q is the finite power dissipation (loss) of the sample itself. In addition, the resonators cannot be

made with metallic walls since metallic objects will interfere with the NMR signal. For these reasons, in present day experiments, power levels in the ten to twenty Watt range are used to saturate the enhancement in DNP NMR experiments. Novel coupling schemes and dielectric cavities could prove useful in the future to raising the *Q* of the sample chambers and alleviating the stringent requirements on the THz power level.

Further utilization of THz DNP NMR will likely be strongly coupled to advances in THz technology. The THz source power level of 10–100 W needed for THz DNP NMR is currently only achievable by gyrotrons. However, one can envision the possibility of achieving the required power levels at THz frequencies with advanced versions of klystrons or traveling wave tubes. These might bring down the cost and complexity of the THz DNP NMR system. When coupled with commercial development, THz DNP NMR could become the preferred approach to many solid and liquid state NMR experiments.

Acknowledgments

This work was supported by the National Institutes of Health through Grants EB001965, EB004866, EB001960, EB002804, EB003151, and EB002026. The work of A. B. Barnes was supported in part by graduate research fellowship from the National Science Foundation.

References

1. Abragam A, Goldman M. Principles of dynamic nuclear polarisation. Rep. Progr. in Phys. 1978; vol. 41(no. 3):395.
2. Overhauser A. Polarization of nuclei in metals. Phys. Rev. 1953; vol. 92:411–415.
3. Carver T, Slichter C. Polarization of nuclear spins in metals. Phys. Rev. 1953; vol. 92:212–213.
4. Abragam A, Proctor WG. A novel method of dynamic polarization of atomic nuclei in solids. CR Acad. Sci. 1959; vol. 246
5. Afeworki M, Mckay RA, Schaefer J. Selective observation of the interface of heterogeneous polycarbonate polystyrene blends by dynamic nuclear-polarization C-13 NMR-spectroscopy. Macromolecules. 1992; vol. 25(no. 16):4084–4091.
6. Singel DJ, Seidel H, Kendrick RD, Yannoni CS. A spectrometer for EPR, DNP, and multinuclear high-resolution NMR. J. Magn. Resonance. 1989; vol. 81:145–161.
7. Wind RA, Duijvestijn MJ, Vanderlugt C, Manenschijn A, Vriend J. Applications of dynamic nuclear-polarization in C-13 NMR in solids. Progr. in Nuclear Mag. Resonance Spectrosc. 1985; vol. 17:33–67.
8. Barnes AB, De Paëpe G, van der Wel PCA, Hu KN, Joo CG, Bajaj VS, Mak-Jurkauskas ML, Sirigiri JR, Herzfeld J, Temkin RJ, Griffin RG. High-field dynamic nuclear polarization for solid and solution biological NMR. Appl. Magn. Resonance. 2008; vol. 34(no. 3):237–263.
9. Griffin RG, Prisner TF. High field dynamic nuclear polarization— The renaissance. Phys. Chem. Chem. Phys. 2010; vol. 12(no. 22):5737–5740. [PubMed: 20485782]
10. Wollan D. Dynamic nuclear polarization with an inhomogeneously broadened ESR line. I theory. Phys. Rev. B. 1976; vol. 13:3671–3685.
11. Wollan DS. Dynamic nuclear polarization with an inhomogeneously broadened ESR line. II. Experiment. Phys. Rev. B. 1976; vol. 13(no. 9):3686.
12. Ardenkjær-Larsen JH, Fridlund B, Gram A, Hansson G, Hansson L, Lerche MH, Servin R, Thaning M, Golman K. Increase in signal-to-noise ratio of 10 000 times in liquid-state NMR. Proc. Nat. Acad. Sci. USA. 2003; vol. 100(no. 18):10158–10163.
13. Becerra LR, Gerfen GJ, Temkin RJ, Singel DJ, Griffin RG. Dynamic nuclear polarization with a cyclotron resonance maser at 5 T. Phys. Rev. Lett. 1993; vol. 71(no. 21):3561–3564. [PubMed: 10055008]
14. Bajaj V, Farrar C, Hornstein M, Mastovsky I, Vieregg J, Bryant J, Elena B, Kreischer K, Temkin R, Griffin R. Dynamic nuclear polarization at 9T using a novel 250 GHz gyrotron microwave source. J. Magn. Resonance. 2003; vol. 160(no. 2):85–90.

15. Hornstein MK, Bajaj VS, Griffin RG, Kreischer KE, Mastovsky I, Shapiro MA, Sirigiri JR, Temkin RJ. Second harmonic operation at 460 GHz and broadband continuous frequency tuning of a gyrotron oscillator. IEEE Trans. Electron Devices. 2005; vol. 52(no. 5):798–807.
16. Torrezan, AC.; Seong-Tae, H.; Shapiro, MA.; Sirigiri, JR.; Temkin, RJ. CW operation of a tunable 330/460 GHz gyrotron for enhanced nuclear magnetic resonance; 2008. 33rd Int. Conf. on Infrared, Millimeter and Terahertz Waves, 2008. IRMMW-THz; p. 1-2.
17. Denysenkov V, Prandolini MJ, Gafurov M, Sezer D, Endeward B, Prisner TF. Liquid state DNP using a 260 GHz high power gyrotron. Physical Chem. Chemical Phys. 2010; vol. 12(no. 22): 5786–5790.
18. Akbey U, Franks WT, Linden A, Lange S, Griffin RG, van Rossum B-J, Oschkinat H. Dynamic nuclear polarization of deuterated proteins. Ang. Chem.Int. Edition. 2010; vol. 49(no. 42):7803–7806.
19. Matsuki Y, Takahashi H, Ueda K, Idehara T, Ogawa I, Toda M, Akutsu H, Fujiwara T. Dynamic nuclear polarization experiments at 14.1 T for solid-state NMR. Physical Chem. Chemical Phys. 2010; vol. 12(no. 22):5799–5803.
20. Rosay M, Tometich L, Pawsey S, Bader R, Schauwecker R, Blank M, Borchard PM, Cauffman SR, Felch KL, Weber RT, Temkin RJ, Griffin RG, Maas WE. Solid-state dynamic nuclear polarization at 263 GHz: Spectrometer design and experimental results. Physical Chem. Chemical Phys. 2010; vol. 12(no. 22):5850–5860.
21. Vitzthum V, Caporini MA, Bodenhausen G. Solid-state nitrogen-14 nuclear magnetic resonance enhanced by dynamic nuclear polarization using a gyrotron. J. Magn. Resonance. 2010; vol. 205(no. 1):177–179.
22. Matsuki Y, Maly T, Ouari O, Karoui H, Le Moigne F, Rizzato E, Lyubenova S, Herzfeld J, Prisner T, Tordo P, Griffin R. Dynamic nuclear polarization with a rigid biradical. Ang. Chem. 2009; vol. 121(no. 27):5096–5100.
23. Joo C-G, Hu K-N, Bryant J, Griffin RG. In situ temperature jump high-frequency dynamic nuclear polarization experiments: Enhanced sensitivity in liquid-state NMR spectroscopy. J. Amer. Chem. Soc. 2006; vol. 128:9428–9432. [PubMed: 16848479]
24. Afeworki M, Mckay RA, Schaefer J. Dynamic nuclear-polarization enhanced nuclear-magnetic-resonance of polymer-blend interfaces. Mater. Sci. Eng.—Structural Mater. Properties Microstructure and Process. 1993; vol. 162(no. 1–2):221–228.
25. Afeworki M, Schaefer J. Mechanism of DNP-enhanced polarization transfer across the interface of polycarbonate/polystyrene heterogeneous blends. Macromolecules. 1992; vol. 25(no. 16):4092–4096.
26. Afeworki M, Vega S, Schaefer J. Direct electron-to-carbon polarization transfer in homgeneously-doped polycarbonates. Macromolecules. 1992; vol. 25(no. 16):4100–4106.
27. Afeworki M, Schaefer J. Molecular dynamics of polycarbonate chains at the interface of polycarbonate/polystyrene heterogeneous blends. Macromolecules. 1992; vol. 25(no. 16):4097–4099.
28. Gerfen GJ, Becerra LR, Hall DA, Griffin RG, Temkin RJ, Singel DJ. High-frequency (140 GHz) dynamic nuclear-polarization— Polarization transfer to a solute in frozen aqueous-solution. J. Chem. Phys. 1995; vol. 102(no. 24):9494–9497.
29. Rosay M, Weis V, Kreischer KE, Temkin RJ, Griffin RG. Two-dimensional 13C-13C correlation spectroscopy with magic angle spinning and dynamic nuclear polarization. J. Amer. Chem. Soc. 2002; vol. 124(no. 13):3214–3215. [PubMed: 11916398]
30. Rosay M, Lansing JC, Haddad K, Bachovchin W, Herzfeld J, Temkin R, Griffin R. High frequency dynamic nuclear polarization in MAS spectra of membrane and soluble proteins. J. Amer. Chem. Soc. 2003; vol. 125:13 626–13 627.
31. Bajaj VS, Hornstein MK, Kreischer KE, Sirigiri JR, Woskov PP, Mak-Jurkauskas ML, Herzfeld J, Temkin RJ, Griffin RG. 250 GHz CW gyrotron oscillator for dynamic nuclear polarization in biological solid state NMR. J. Magn. Resonance. 2007; vol. 189(no. 2):251–279.
32. Maly T, Debelouchina GT, Bajaj VS, Hu K-N, Joo C-G, Mak-Jurkauskas ML, Sirigiri JR, v. d. Wel PCA, Herzfeld J, Temkin RJ, Griffin RG. Dynamic nuclear polarization at high magnetic fields. J. Chem. Phys. 2008; vol. 128:052211. [PubMed: 18266416]

33. Goldman, M. Spin Temperature and Nuclear Magn. Resonance in Solids. Oxford, U.K.: Oxford Univ. Press; 1970.
34. Hu K-N, Bajaj VS, Rosay MM, Griffin R. High frequency dynamic nuclear polarization using mixtures of TEMPO and trityl radicals. J. Chem. Phys. 2007; vol. 126:044512. [PubMed: 17286492]
35. Hu K-N, Yu H-H, Swager TM, Griffin RG. Dynamic nuclear polarization with biradicals. J. Amer. Chem. Soc. 2004; vol. 126(no. 35):10 844–10 845.
36. Atsarkin V. Dynamic polarization of nuclei in solid dielectrics. Sov. Phys. Solid State. 1978; vol. 21:725–744.
37. van der Wel P, Hu K-N, Lewandowski JR, Griffin R. Dynamic nuclear polarization of amyloidogenic peptide nanocrystals: GNNQQNY, a core segment of the yeast prion protein sup35p. J. Amer. Chem. Soc. 2006; vol. 128:10 840–10 846.
38. Debelouchina G, Bayro M, van der Wel P, Caporini M, Barnes A, Rosay M, Maas W, Griffin R. Dynamic nuclear polarizationenhanced solid-state NMR spectroscopy of GNNQQNY nanocrystals and amyloid fibrils. Phys. Chem. Chem. Phys. 2010; vol. 12:5911–5919. [PubMed: 20454733]
39. Rosay M, Zeri AC, Astrof NS, Opella SJ, Herzfeld J, Griffin RG. Sensitivity-enhanced NMR of biological solids: Dynamic nuclear polarization of Y21M fd bacteriophage and purple membrane. J. Amer. Chem. Soc. 2001; vol. 123(no. 5):1010–1011. [PubMed: 11456650]
40. Lesage A, Lelli M, Gajan D, Caporini MA, Vitzthum V, Mieville P, Alauzun J, Roussey A, Thieuleux C, Mehdi A, Bodenhausen G, Coperet C, Emsley L. Surface enhanced NMR spectroscopy by dynamic nuclear polarization. J. Amer. Chem. Soc. 2010; vol. 132(no. 44):15 459–15 461.
41. Tycko R. Progress towards a molecular-level structural understanding of amyloid fibrils. Current Opinion in Structural Biol. 2004; vol. 14(no. 1):96–103.
42. Chiti F, Dobson CM. Protein misfolding, functional amyloid, and human disease. Annu. Rev. Biochem. 2006; vol. 75(no. 1):333–366. [PubMed: 16756495]
43. Jaroniec C, MacPhee C, Astrof N, Dobson C, Griffin R. Molecular conformation of a peptide fragment of transthyretin in an amyloid fibril. Proc. Nat. Acad. Sci. 2002; vol. 99:16 748–16 753.
44. van der Wel PCA, Lewandoswki J, Griffin RG. Solid state NMR study of amyloid nanocrystals and fibrils formed by the peptide GNNQQNY from yeast prion protein sup35p. J. Amer. Chem. Soc. 2007; vol. 128(no. 33):10 840–10 846.
45. Barnes AB, Mak-Jurkauskas ML, Matsuki Y, Bajaj VS, van der Wel PCA, DeRocher R, Bryant J, Sirigiri JR, Temkin RJ, Lugtenburg J, Herzfeld J, Griffin RG. Cryogenic sample exchange NMR probe for magic angle spinning dynamic nuclear polarization. J. Magn. Res. 2009; vol. 198(no. 2): 261–270.
46. Griffiths J, Lakshmi K, Bennett A, Raap J, Vanderwielen C, Lugtenburg J, Herzfeld J, Griffin R. Dipolar correlation NMR-spectroscopy of a membrane-protein. J. Amer. Chem. Soc. 1994; vol. 116(no. 22):10 178–10 181.
47. Bajaj V, Mak-Jurkauskas M, Belenky M, Herzfeld J, Griffin R. Functional and shunt states of bacteriorhodopsin resolved by 250 GHz dynamic nuclear polarizationenhanced solid-state NMR. Proc. Nat. Acad. Sci. 2009; vol. 106(no. 23):9244. [PubMed: 19474298]
48. Lanyi JK, Schobert B. Crystallographic structure of the retinal and the protein after deprotonation of the Schiff base: The switch in the bacteriorhodopsin photocycle. J. Mol. Biol. 2002; vol. 321(no. 4):727–737. [PubMed: 12206786]
49. Barnes AB, Corzilius B, Mak-Jurkauskas ML, Andreas LB, Bajaj VS, Matsuki Y, Belenky ML, Lugtenburg J, Sirigiri JR, Temkin RJ, Herzfeld J, Griffin RG. Resolution and polarization distribution in cryogenic DNP/MAS experiments. Physical Chem. Chemical Phys. 2010; vol. 12(no. 22):5861–5867.
50. Granatstein VL, Parker RK, Armstrong CM. Vacuum electronics at the dawn of the Twenty-First century. Proc. IEEE. 1999; vol. 87(no. 5):702–716.
51. Thurber KR, Yau W-M, Tycko R. Low-temperature dynamic nuclear polarization at 9.4 T with a 30 mW microwave source. J. Magn. Resonance. 2010; vol. 204(no. 2):303–313.
52. Weis V, Bennati M, Rosay M, Bryant JA, Griffin RG. High-field DNP and ENDOR with a novel multiple-frequency resonance structure. J. Magn. Resonance. 1999; vol. 140(no. 1):293–299.

53. Prandolini MJ, Denysenkov VP, Gafurov M, Lyubenova S, Endeward B, Bennati M, Prisner TF. First DNP results from a liquid water-TEMPOL sample at 400 MHz and 260 GHz. Appl. Magn. Resonance. 2008; vol. 34(no. 3):399–407.
54. Roitman A, Berry D, Steer B. State-of-the-art W-band extended interaction klystron for the CloudSat program. IEEE Trans. Electron Devices. May; 2005 vol. 52(no. 5):895–898.
55. Steer, B.; Hyttinen, M.; Roitman, A.; Horoyski, P.; Smith, GM.; Bolton, DR.; Cruickshank, PAS.; Robertson, DA. Compact, high power EIK sources used for ESR and NMR; 2008. 33rd Int. Conf. on Infrared, Millimeter and Terahertz Waves (IRMMW-THz'08); p. 1-2.
56. Felch KL, Danly BG, Jory HR, Kreischer KE, Lawson W, Levush B, Temkin RJ. Characteristics and applications of fast-wave gyrodevices. Proc. IEEE. 1999; vol. 87(no. 5):752–781.
57. Nusinovich, G. Introduction to the Physics of Gyrotrons. Baltimore, MD: Johns Hopkins Univ. Press; 2004.
58. Zapevalov, VE.; Dubrov, VV.; Fix, AS.; Kopelovich, EA.; Kuftin, AN.; Malygin, OV.; Manuilov, VN.; Moiseev, MA.; Sedov, AS.; Venediktov, NP.; Zavolsky, NA. Development of 260 GHz second harmonic CW gyrotron with high stability of output parameters for DNP spectroscopy; 34th Int. Conf. on Infr., Millim., and Terahertz Waves (IRMMW-THz'09); p. 1-2.
59. Kosuga, K.; Idehara, T.; Ogawa, I.; Saito, T.; Agusu, L.; Kanemaki, T.; Smith, ME.; Dupree, R. Development of gyrotron FU CW VII for 600 and 300 MHz DNP-NMR; 34th Int. Conf. on Infr., Millim., and Terahertz Waves (IRMMW-THz'09); p. 1-2.
60. Torrezan AC, Shapiro MA, Sirigiri JR, Temkin RJ, Griffin RG. Operation of a continuously frequency-tunable second-harmonic CW 330-GHz gyrotron for dynamic nuclear polarization. IEEE Trans. Electron Devices. Aug; 2011 vol. 58(no. 8):2777–2783.
61. Danly B, Temkin R. Generalized nonlinear harmonic gyrotron theory. Phys. Fluids. 1986; vol. 29(no. 2):561.
62. Twiss R. Radiation transfer and the possibility of negative absorption in radio astronomy. Australian J. Physi. 1958; vol. 11(no. 4):564–579.
63. Schneider J. Stimulated emission of radiation by relativistic electrons in a magnetic field. Physical Review Letters. 1959; vol. 2(no. 12):504–505.
64. Gapanov A. Addendum izvestia. Izv. VUZ. Radiofiz. 1959; vol. 2:450–462.
65. Hirshfield JL, Wachtel JM. Electron cyclotron maser. Phys. Rev. Lett. 1964; vol. 12:533–536.
66. Zaytsev N, Pankratova T, Petelin M, Flyagin V. Millimeterand submillimeter-wave gyrotrons. Radio Eng. Electron. Phys. 1974; vol. 19(no. 5):103–107.
67. Temkin RJ, Kreischer KE, Mulligan WJ, MacCabe S, Fetterman HR. A 100 kW: 140 GHz pulsed gyrotron. Int. J. Infr. Millim. Waves. 1982; vol. 3(no. 4):427–437.
68. Spira-Hakkarainen S, Kreischer KE, Temkin RJ. Submillimeter-wave harmonic gyrotron experiment. IEEE Trans. Plasma Science. Jun; 1990 vol. 18(no. 3):334–342.
69. Notake T, Saito T, Tatematsu Y, Fujii A, Ogasawara S, Agusu L, Ogawa I, Idehara T, Manuilov VN. Development of a novel high power sub-THz second harmonic gyrotron. Phys. Rev. Lett. 2009; vol. 103(no. 22):225002. [PubMed: 20366101]
70. Grimm TL, Kreischer KE, Temkin RJ. Experimental study of a megawatt 200–300 GHz gyrotron oscillator. Phys. Fluids B. 1993; vol. 5(no. 11):4135–4143.
71. Temkin R, Kreischer K, Wolfe S, Cohn D, Lax B. High frequency gyrotrons and their application to tokamak plasma heating. J. Mag. Magn. Materials. 1979; vol. 11(no. 1–3):368–371.
72. Thumm M. State-of-the-art of high power gyro-devices and free electron masers update 2002. Wissenschaftliche Berichte FZKA. 2003; vol. 6815:1–83.
73. Brand GF, Chen Z, Douglas NG, Gross M, Ma JYL, Robinson LC. A tunable millimeter submillimeter gyrotron. Int. J. Electron. 1984; vol. 57(no. 863)
74. Idehara, T.; Ogawa, I.; Mori, H.; Kobayashi, S.; Mitsudo, S.; Saito, T. A THz gyrotron FU CW III with a 20 T superconducting magnet; 2008 33rd Int. Conf. on Infrared, Millimeter and Terahertz Waves; p. 1-2.
75. Idehara T, Misudo S, Ogawa I. Development of high-frequency, highly stable gyrotrons as millimeter to submillimeter wave radiation sources. IEEE Trans. Plasma Sci. Jun; 2004 vol. 32(no. 3):910–916.

76. Booske JH, Dobbs RJ, Joye CD, Kory CL, Neil GR, Park G-S, Park J, Temkin RJ. Vacuum electronic high power terahertz sources. IEEE Trans. THz Sci. Tech. Sep.2011 vol. 1(no. 1)
77. Joye CD, Griffin RG, Hornstein MK, Kan-Nian H, Kreischer KE, Rosay M, Shapiro MA, Sirigiri JR, Temkin RJ, Woskov PP. Operational characteristics of a 14-W 140-GHz gyrotron for dynamic nuclear polarization. IEEE Trans. Plasma Sci. Jun; 2006 vol. 34(no. 3):518–523.
78. Han ST, Griffin RG, Hu K-N, Joo C-G, Joye CD, Mastovsky I, Shapiro MA, Sirigiri JR, Temkin RJ, Torrezan AC, Woskov PP. Continuous-wave submillimeter-wave gyrotrons. Proc. SPIE. 2006; vol. 6373:539–540.
79. Han S, Joye C, Mastovsky L, Shapiro M, Sirigiri J, Temkin R, Woskov P. Stable operation of a 0.46 THz continuous wave gyrotron oscillator. 2006 IEEE Int. Vacuum Electron. Conference. 2006:06EX1278.
80. Kreischer, K.; Farrar, C.; Griffin, R.; Temkin, R.; Vieregg, J. A 250 GHz gyrotron for NMR spectroscopy; 27th Int. IEEE Plasma Sci. Conf. Rec.—Abstracts (ICOPs'00); 2000. p. 198
81. Woskov PP, Bajaj VS, Hornstein MK, Temkin RJ, Griffin RG. Corrugated waveguide and directional coupler for CW 250-GHz gyrotron DNP experiments. IEEE Trans. Microw. Theory Techn. Jun; 2005 vol. 53(no. 6):1863–1869.
82. Nanni EA, Barnes AB, Matsuki Y, Woskov PP, Corzilius B, Griffin RG, Temkin RJ. Microwave field distribution in a magic angle spinning dynamic nuclear polarization NMR probe. J. Magn. Resonance. 2011; vol. 210(no. 1):16–23.
83. Hornstein M, Bajaj V, Griffin R, Temkin RJ. Continuous-wave operation of a 460-GHz second harmonic gyrotron oscillator. IEEE Trans. Plasma Sci. Jun; 2006 vol. 34(no. 3):524–533.
84. Denysenkov V, Kiseliov V, Prandolini M, Gafurov M, Krahn A, Engelke F, Bezborodov V, Kuleshov Y, Nesterov P, Yanovsky M, Prisner T. 260 GHz quasioptical setup for EPR and DNP experiments on the 9.2 tesla DNP/NMR/EPR spectrometer. 2010 Int. Kharkov Symp. Phys. Eng. Microw., Millim. and Submillim. Waves (MSMW). 2010:1–7.
85. Ikeda, R.; Idehara, T.; Ogawa, I.; Kosuga, K.; Saito, T.; Matsuki, Y.; Ueda, K.; Fujiwara, T.; Chang, TH. Development of continuously frequency tunable gyrotrons FU CW VI and FU CW VI A for application to 600 MHz DNP-NMR spectroscopy; 2010 35th Int. Conf. Infrared Millimeter and Terahertz Waves (IRMMW-THz); p. 1-2.
86. Idehara T, Kosuga K, Agusu L, Ikeda R, Ogawa I, Saito T, Matsuki Y, Ueda K, Fujiwara T. Continuously frequency tunable high power sub-THz radiation sourcegyrotron FUCW VI for 600 MHz DNP-NMR spectroscopy. J. Infrar., Millim. Terahertz Waves. 2010; vol. 31(no. 7):775–790.
87. Vlasov SN, Orlova IM. Quasioptical transformer which transforms the waves in a waveguide having a circular cross section into a highly directional wave beam. Radiophys. Quantum Electron. 1974; vol. 17(no. 1):115–119.
88. Choi E, Shapiro M, Sirigiri J, Temkin R. Calculation of radiation from a helically cut waveguide for a gyrotron mode converter in the quasi-optical approximation. J. Infrared, Millim. TerahertzWaves. 2009; vol. 30(no. 1):8–25.
89. Neilson JM, Bunger R. Surface integral equation analysis of quasi-optical launchers. IEEE Trans. Plasma Si. Jun; 2002 vol. 30(no. 3):794–799.
90. Torrezan AC, Seong-Tae H, Mastovsky I, Shapiro MA, Sirigiri JR, Temkin RJ, Barnes AB, Griffin RG. Continuous-wave operation of a frequency-tunable 460-GHz second-harmonic gyrotron for enhanced nuclear magnetic resonance. IEEE Trans. Plasma Si. Jun; 2010 vol. 38(no. 6):1150–1159.
91. Bhartia, P.; Bahl, I. Transmission Lines 1 Waveguides. Hoboken, NJ: Wiley; 1984. ch. 5
92. Thumm MK, Kasparek W. Passive high-power microwave components. IEEE Trans. Plasma Sci. 2002; vol. 30(no. 3):755–786.
93. Doane, JL. Propagation and Mode Coupling in Corrugated and Smooth-Walled Circular Waveguides, ser. Infrared and Millimeter Waves. Vol. vol. 13. New York: Academic; 1985.
94. Kowalski EJ, Tax DS, Shapiro MA, Sirigiri JR, Temkin RJ, Bigelow TS, Rasmussen DA. Linearly polarized modes of a corrugated metallic waveguide. IEEE Trans. Microw. Theory Techn. Nov; 2010 vol. 58(no. 11):2772–2780.

95. Shapiro MA, Kowalski EJ, Sirigiri JR, Tax DS, Temkin RJ, Bigelow TS, Caughman JB, Rasmussen DA. Loss estimate for ITER ECH transmission line including multimode propagation. Fusion Sci. Tech. 2010; vol. 57(no. 3):196–207.
96. Bogdashov, AA.; Belousov, VI.; Chirkov, AV.; Denisov, GG.; Kornishin, SY.; Tai, EM. Transmission line for 258 GHz gyrotron dnp spectroscopy; 2010 35th Int. Conf. on Infr. Millim. Terahertz Waves (IRMMW-THz); p. 1-2.
97. Denisov G, Chirkov A, Belousov V, Bogdashov A, Kalynova G, Sobolev D, Rodin Y, Tai E, Ilin V, Kornishin S, Kulygin M, Malygin V, Soluyanova E, Parshin V, Shmelev M. Millimeter wave multi-mode transmission line components. J. Infr. Millim. Terahertz Waves. 2011:1–15.
98. Ogawa, I.; Idehara, T.; Myodo, M.; Ando, H.; Wagner, D.; Thumm, M. Development of a quasi-optical transmission system for gyrotron application as a radiation source; 2006 Joint 31st Int Conf. on Infr. Millim. Waves and 14th Int. Conf. on Teraherz Electron.. (IRMMWTHz); p. 552-552.
99. Bajaj VS, van der Wel PCA, Griffin RG. Observation of a low-temperature, dynamically driven structural transition in a polypeptide by solid-state NMR spectroscopy. J. the American Chemical Society. 2008; vol. 131(no. 1):118–128.
100. Mak-Jurkauskas M, Bajaj V, Hornstein M, Belenky M, Temkin RJ, Griffin R, Herzfeld J. Energy transformations early in the bacteriorhodopsin photocycle revealed by DNP-enhanced solid state NMR. Proc. Nat. Acad. Sci. USA. 2008; vol. 105(no. 3):883–888. [PubMed: 18195364]
101. McKay, RA. Double-tuned single coil probe for nuclear magnetic resonance spectrometer. U.S. U.S. Patent. 4 446 431. 1984 May 1.
102. McKay, R. Probes for Special Purposes. Vol. vol. 6. New York: John Wiley and Sons; 1996. p. 3768-3771.
103. Macor, A.; de Rijk, E.; Boero, G.; Ansermet, JP.; Alberti, S. Millimeter waves for NMR enhancement; 2010 35th Int. Conf. on Infr. Millim. Terahertz Waves (IRMMW-THz); p. 1-2.
104. Denysenkov VP, Prandolini MJ, Krahn A, Gafurov M, Endeward B, Prisner TF. High-field DNP spectrometer for liquids. Appl. Magn. Resonance. 2008; vol. 34(no. 3):289–299.
105. Annino G, Villanueva-Garibay J, van Bentum P, Klaassen A, Kentgens A. A high-conversion-factor, double-resonance structure for high-field dynamic nuclear polarization. Appl. Magn. Resonance. 2010; vol. 37(no. 1):851–864.
106. Hu K-N, Song C, Yu H-H, Swager TM, Griffin RG. Highfrequency dynamic nuclear polarization using biradicals: A multifrequency EPR lineshape analysis. J. Chem. Phys. 2008; vol. 128:052321.
107. Song C, Hu K-N, Joo C-G, Swager T, Griffin R. TOTAPOL a biradical polarizing agent for dynamic nuclear polarization experiments in aqueous media. J. Amer. Chem. Soc. 2006; vol. 128:11 385–11 390.
108. Alberti, S.; Ansermet, JP.; Avramides, KA.; Fasel, D.; Hogge, JP.; Kern, S.; Lievin, C.; Liu, Y.; Macor, A.; Pagonakis, I.; Silva, M.; Tran, MQ.; Tran, TM.; Wagner, D. Design of a frequency-tunable gyrotron for DNP-enhanced NMR spectroscopy; 2009 34th Int. Conf. on Infrared, Millimeter, and Terahertz Waves (IRMMW-THz); p. 1-2.
109. Krahn A, Lottmann P, Marquardsen T, Tavernier A, Turke M-T, Reese M, Leonov A, Bennati M, Hoefer P, Engelke F, Griesinger C. Shuttle DNP spectrometer with a two-center magnet. Phys. Chem. Chemical Phys. 2010; vol. 12(no. 22):5830–5840.
110. Leggett J, Hunter R, Granwehr J, Panek R, Perez-Linde AJ, Horsewill AJ, McMaster J, Smith G, Kockenberger W. A dedicated spectrometer for dissolution DNP NMR spectroscopy. Phys. Chem. Chemical Phys. 2010; vol. 12(no. 22):5883–5892.
111. Bennati M, Luchinat C, Parigi G, Turke M-T. Water 1H relaxation dispersion analysis on a nitroxide radical provides information on the maximal signal enhancement in overhauser dynamic nuclear polarization experiments. Phys. Chem. Chemical Phys. 2010; vol. 12(no. 22): 5902–5910.
112. Armstrong BD, Edwards DT, Wylde RJ, Walker SA, Han S. A 200 GHz dynamic nuclear polarization spectrometer. Phys. Chem. Chemical Phys. 2010; vol. 12(no. 22):5920–5926.

Biographies

Emilio A. Nanni (S'09) received the B.S. degrees in electrical engineering and in physics from the University of Missouri, Rolla, in 2007, and the S.M. degree in electrical engineering from the Massachusetts Institute of Technology, Cambridge, in 2010, where he is currently working toward the Ph.D. degree.

In 2008, he was with the NASA Marshall Space Flight Center developing non-destructive evaluation techniques for applications related to the US space program. He is currently a Graduate Research Assistant with the Waves and Beams Division of the Plasma Science and Fusion Center, MIT. His research interests include high-power, high-frequency vacuum electronic devices and their application to dynamic nuclear polarization/NMR.

Alexander B. Barnes (S'10) received the B.A. degree in chemistry from Whitman College, Walla Walla, WA, in 2003, and the Ph.D. degree in physical chemistry at the Massachusetts Institute of Technology (MIT), Cambridge, in 2011.

Since 2004, he has been a member of the Francis Bitter Magnet Laboratory, MIT, where he is developing dynamic nuclear polarization-enhanced solid-state nuclear magnetic resonance as a biomolecular structure determination technique. He is now also affiliated with the Waves and Beams division at the Plasma Science and Fusion Center and has taken an active role developing gyrotron technology.

Robert G. Griffin received the B.S. degree in chemistry from the University of Arkansas, Fayetteville, in 1964 and the Ph.D. degree in physical chemistry from Washington University, St. Louis, MO, in 1969.

He did his Post-Doctoral research in physical chemistry at the Massachusetts Institute of Technology (MIT), Cambridge, with Prof. J. S. Waugh. In 1972, after completing his Post-Doctoral training, he assumed a staff position with the Francis Bitter Magnet Laboratory (FBML), MIT. In 1984, he was promoted to Senior Research Scientist. In 1989, he was appointed to the faculty with the Department of Chemistry, MIT. In 1992, he became the Director of FBML and is concurrently the Director of the Harvard Center for Magnetic Resonance, MIT, where he has been the Associate Director since 1989. He has published more than 300 articles concerned with magnetic resonance methodology and applications of

magnetic resonance (NMR and EPR) to studies of the structure and function of a variety of chemical, physical, and biological systems. In the last decade, his research has focused on the development of methods to perform structural studies of membrane and amyloid proteins and on the utilization of high-frequency (>100 GHz) microwaves in EPR experiments and in the development of dynamic nuclear polarization/NMR experiments at these frequencies. He has served on numerous advisory and review panels for the National Science Foundation and the National Institutes of Health.

Richard J. Temkin (M’87-SM’92-F’94) received the B.A. degree in physics from Harvard College, Harvard University, Cambridge, MA, and the Ph.D. degree in physics from the Massachusetts Institute of Technology (MIT), Cambridge.

From 1971 to 1974, he was a Postdoctoral Research Fellow with the Division of Engineering and Applied Physics, Harvard University. Since 1974, he has been with MIT, first with the Francis Bitter Magnet Laboratory and later with the Plasma Science and Fusion Center (PSFC) and the Department of Physics, where he is currently a Senior Scientist with the Department of Physics, the Associate Director of PSFC, and the Head of the Waves and Beams Division, PSFC. He has been the author or coauthor of over 200 published journal articles and book chapters and has been the Editor of six books and conference proceedings. His research interests include novel vacuum electron devices such as gyrotrons and free-electron lasers; advanced high-gradient electron accelerators; overmoded waveguides and antennas at millimeter/terahertz wavelengths; high-power microwave sources and their applications; plasma heating; and dynamic nuclear polarization/NMR.

Dr. Temkin is a Fellow of the American Physical Society and the Institute of Physics, London, U.K. He has been the recipient of the Kenneth J. Button Prize and Medal of the Institute of Physics, London, and the Robert L. Woods Award of the Department of Defense for Excellence in Vacuum Electronics research.

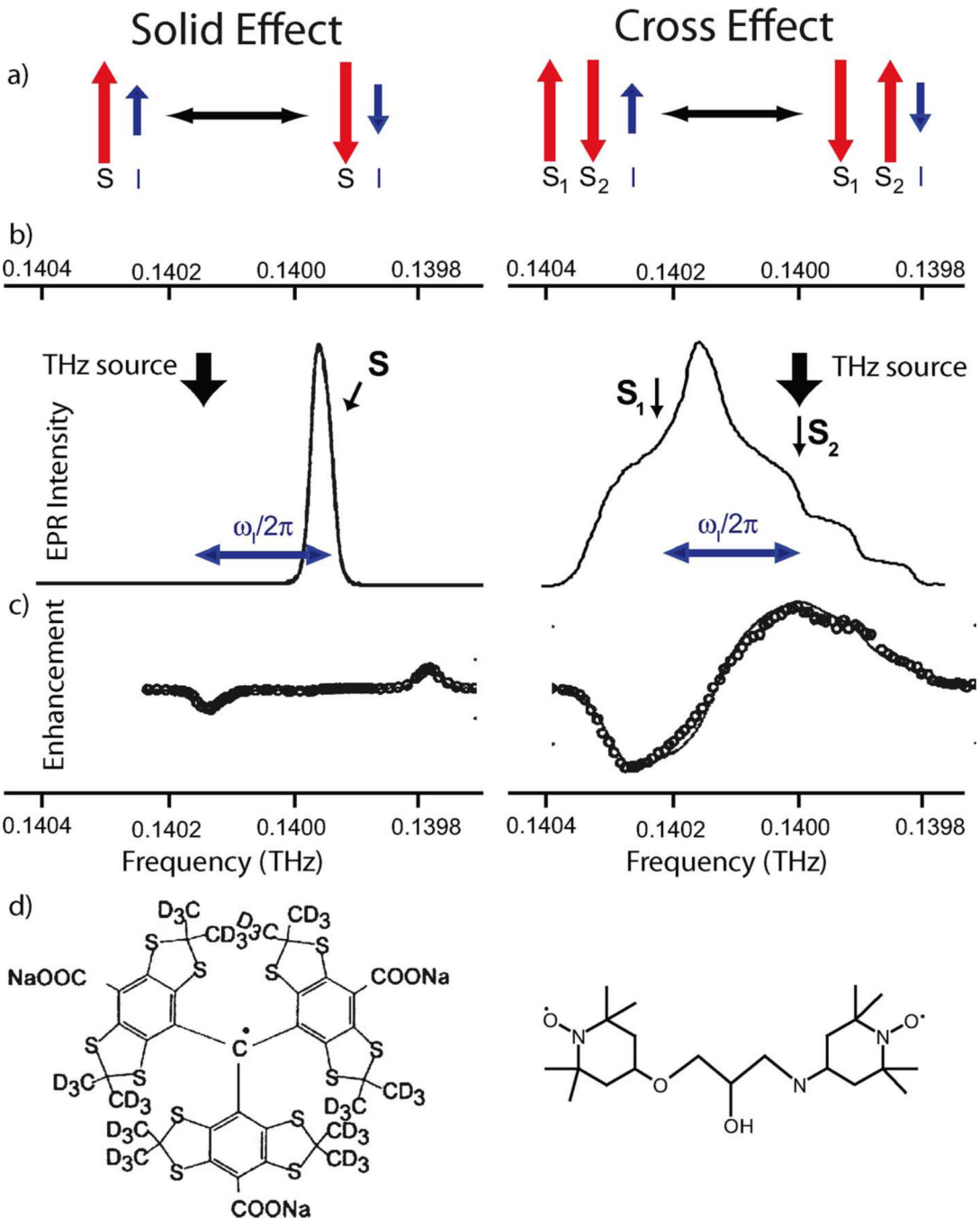

Fig. 1.

Common DNP polarization transfer mechanisms in solid dielectrics. (a) In the SE, one electron and one nuclear spin flip simultaneously with excitation from THz radiation, whereas the CE involves two electron spins and one nuclear spin. (b) EPR spectra of the radicals that are the polarization source in THz DNP experiments. (left) The SE utilizes narrow line radicals such as trityl. (right) EPR spectra of nitroxide radicals such as TEMPO or TOTAPOL are much broader and used for the CE. (c) Field/frequency dependent profiles of the two mechanisms. In the SE (left) the THz source is set to ω_{0I} away from the center of the EPR line. (right) For the CE, the THz radiation is on resonance with one of the two electrons involved. (d) Chemical structures of typical radicals used for the SE; trityl (left)

has a mostly isotropic environment around the unpaired electron density which results in a similar resonance frequency (narrow line) across the powder average of the crystallites. TOTAPOL (right) for the CE, more anisotropic chemical environments around the electron density yield broader lines such that two electrons are separated by ω_{0I} and fulfill the matching condition. (Adapted from [34]).

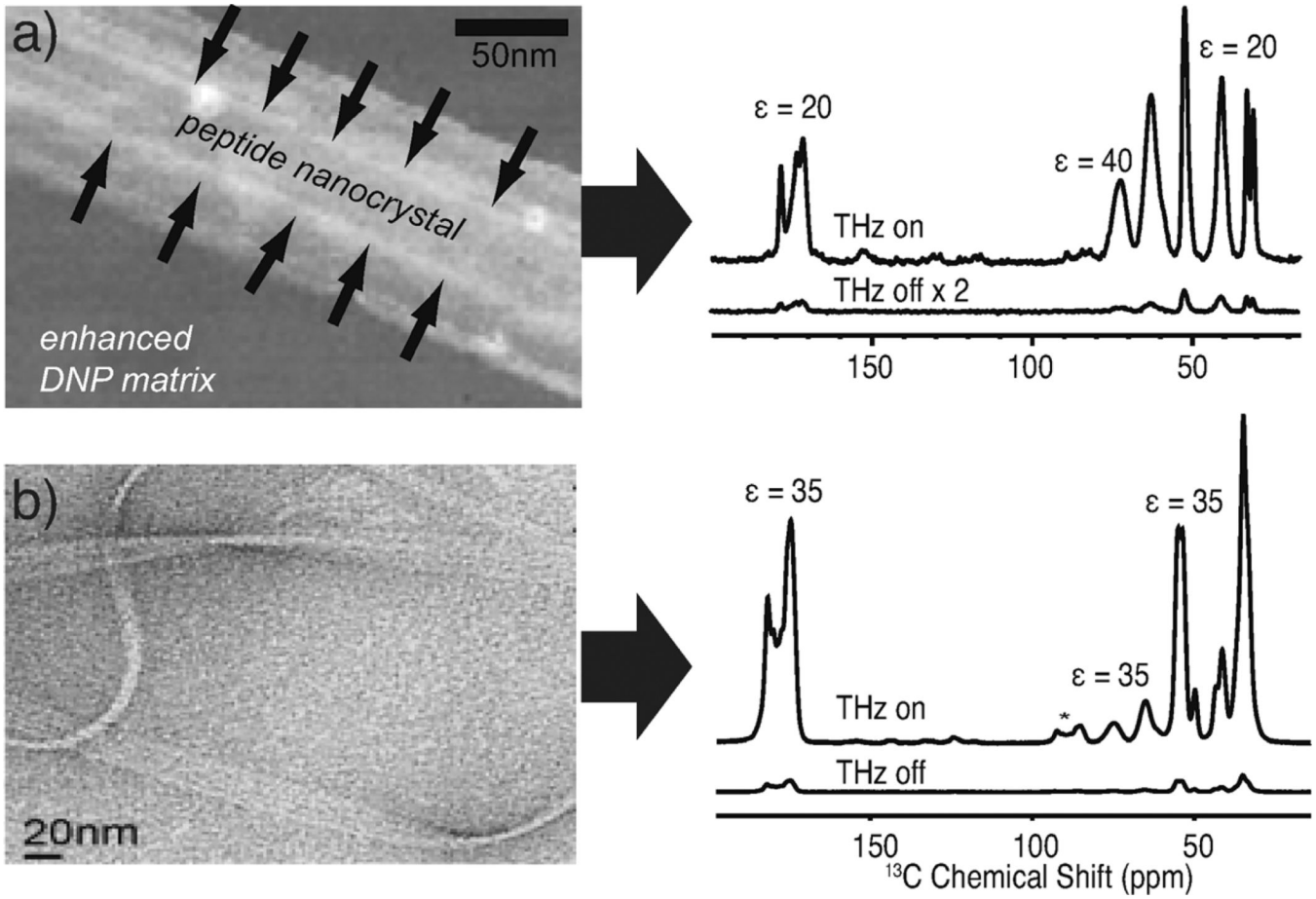

Fig. 2.
Electron micrographs and 0.263 THz DNP spectra of GNNQQNY showing a signal enhancement of (a) 20 on the nanocrystals and (b) 35 on the amyloid fibrils. (Adapted from [37], [44], [38]).

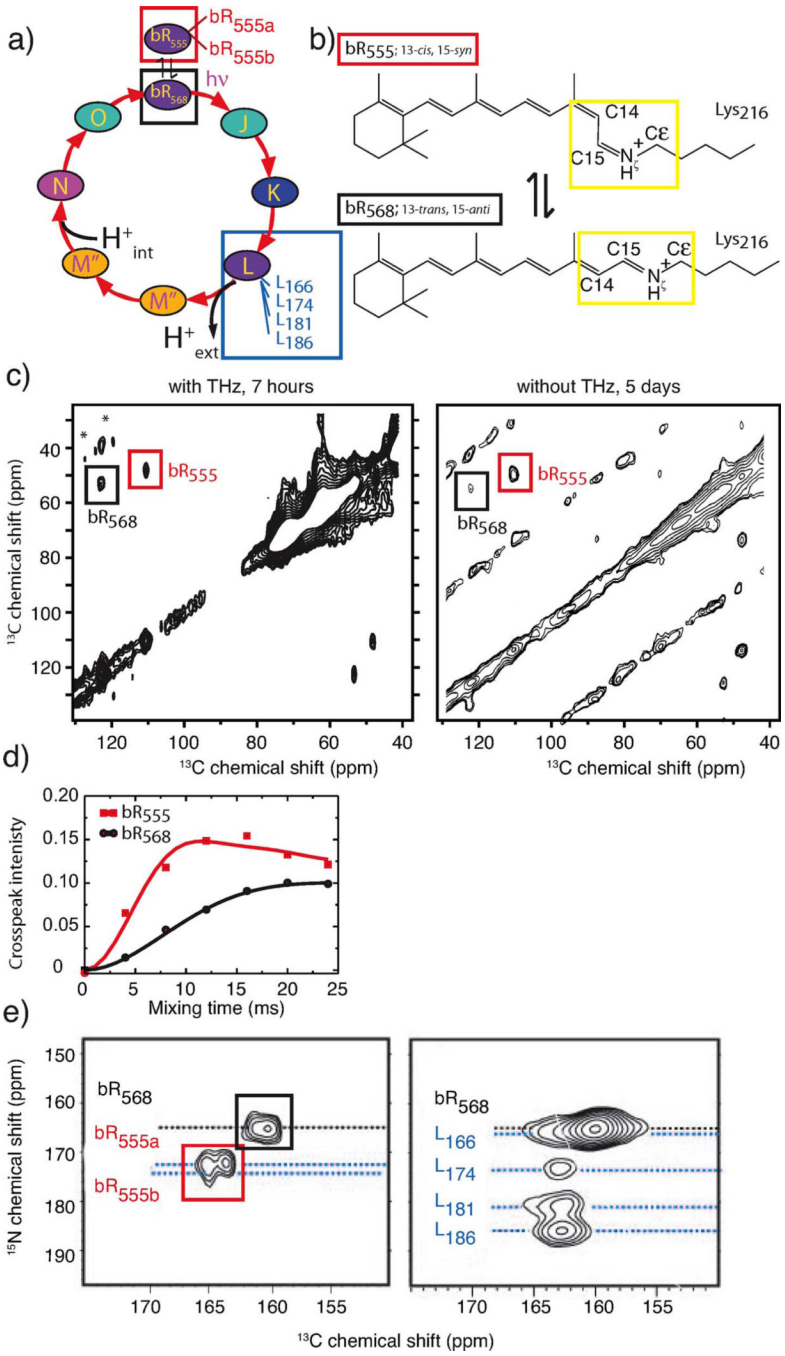

Fig. 3.

(a) Photocycle illustrating the intermediates examined with DNP enhanced MAS spectra. (b) The conformational equilibrium of the retinal chromophore in the resting state. The yellow box highlights the nuclei in the spectra in the lower panels. (c) 2D spectra of the active site of bR showing correlation peaks between C14 and C_ε recorded in 7 hours with THz DNP and 5 days without THz DNP even with 10 times more sample. (d) Build-up profiles of the correlation between C14 and C_ε. The profiles are fit and yield a distance of 3.11 ± 0.22 Å between the C14 and C_ε in bR_{555} and 3.90 ± 0.08 Å in the bR_{568} trans conformation. (e) $^{15}N\zeta$-$^{13}C15$ correlation experiments provide assignments of the retinal-C15 resonance in

each state: (left) the dark-adapted state; (right) the mixture of L intermediates. (Adapted from [45]–[47]).

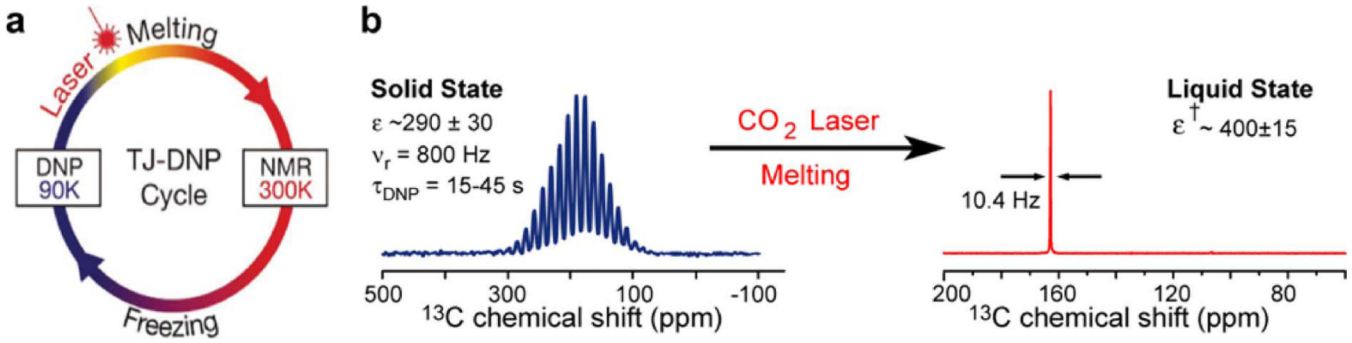

Fig. 4.

(a) Conceptual representation of the TJ-DNP experiment showing the four stages associated with acquisition of a DNP enhanced liquid state spectrum. (b) MAS spectrum produced at 90 K, $\varepsilon \sim 290$ from a urea sample and the resulting liquid state spectrum with an enhancement $\varepsilon^{\dagger} \sim 400$. (Adapted from [23]).

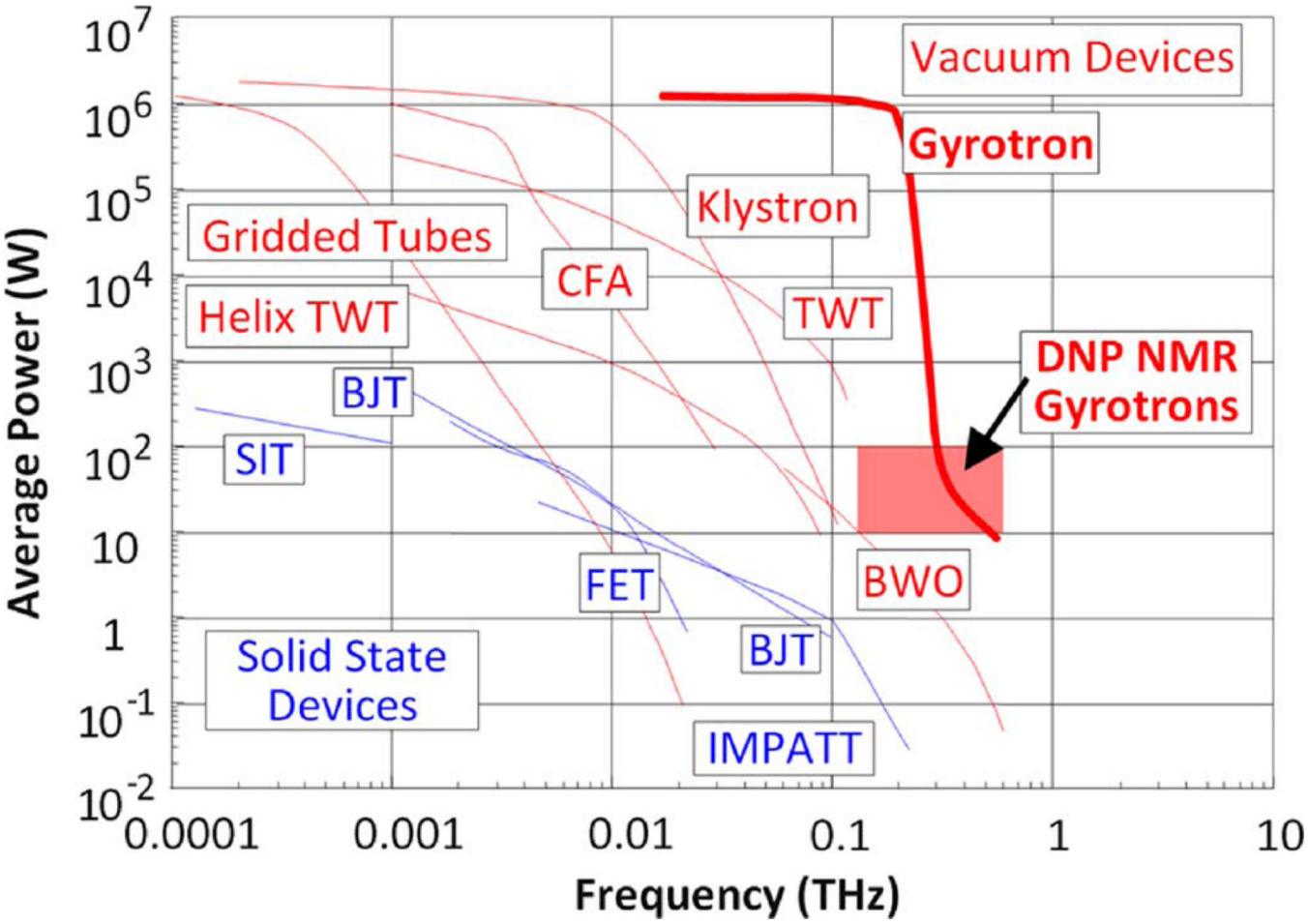

Fig. 5.
State-of-the-art of solid state and vacuum electron devices. (Adapted from [50]).

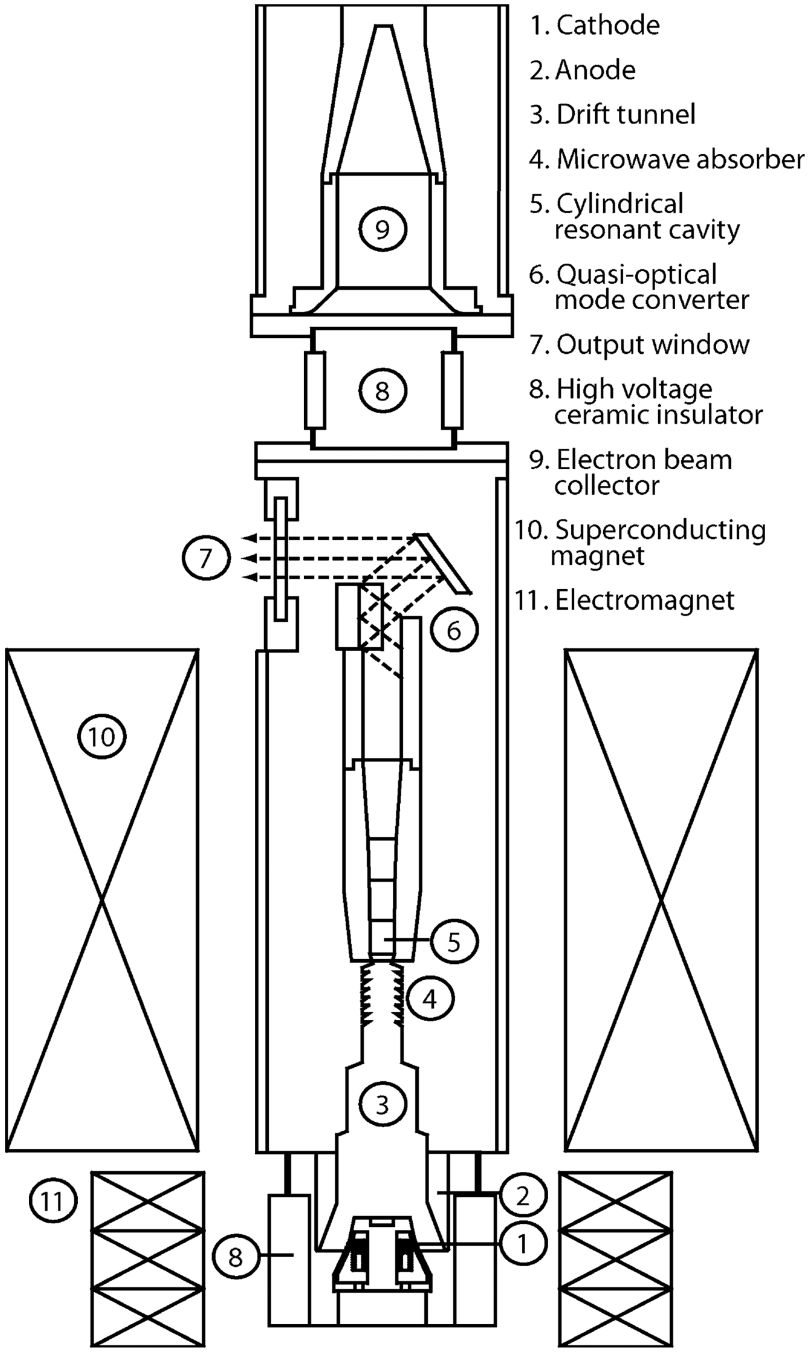

Fig. 6.
Cross-sectional schematic of a typical cylindrically symmetric gyrotron tube used in DNP NMR experiments, not shown to scale, indicating key components. (Adapted from [15]).

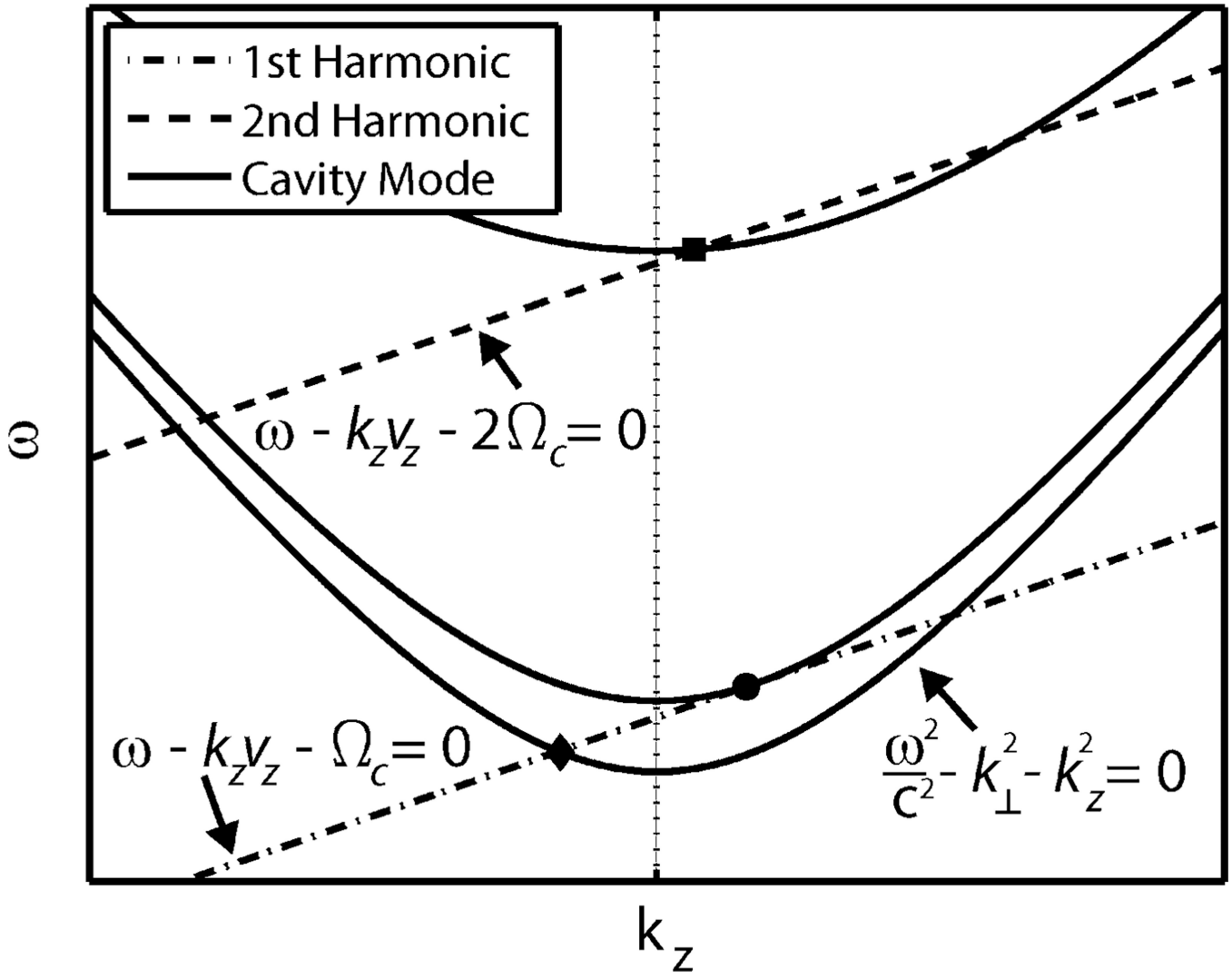

Fig. 7.
Dispersion diagram for the Doppler shifted cyclotron resonance and cylindrical cavity modes.

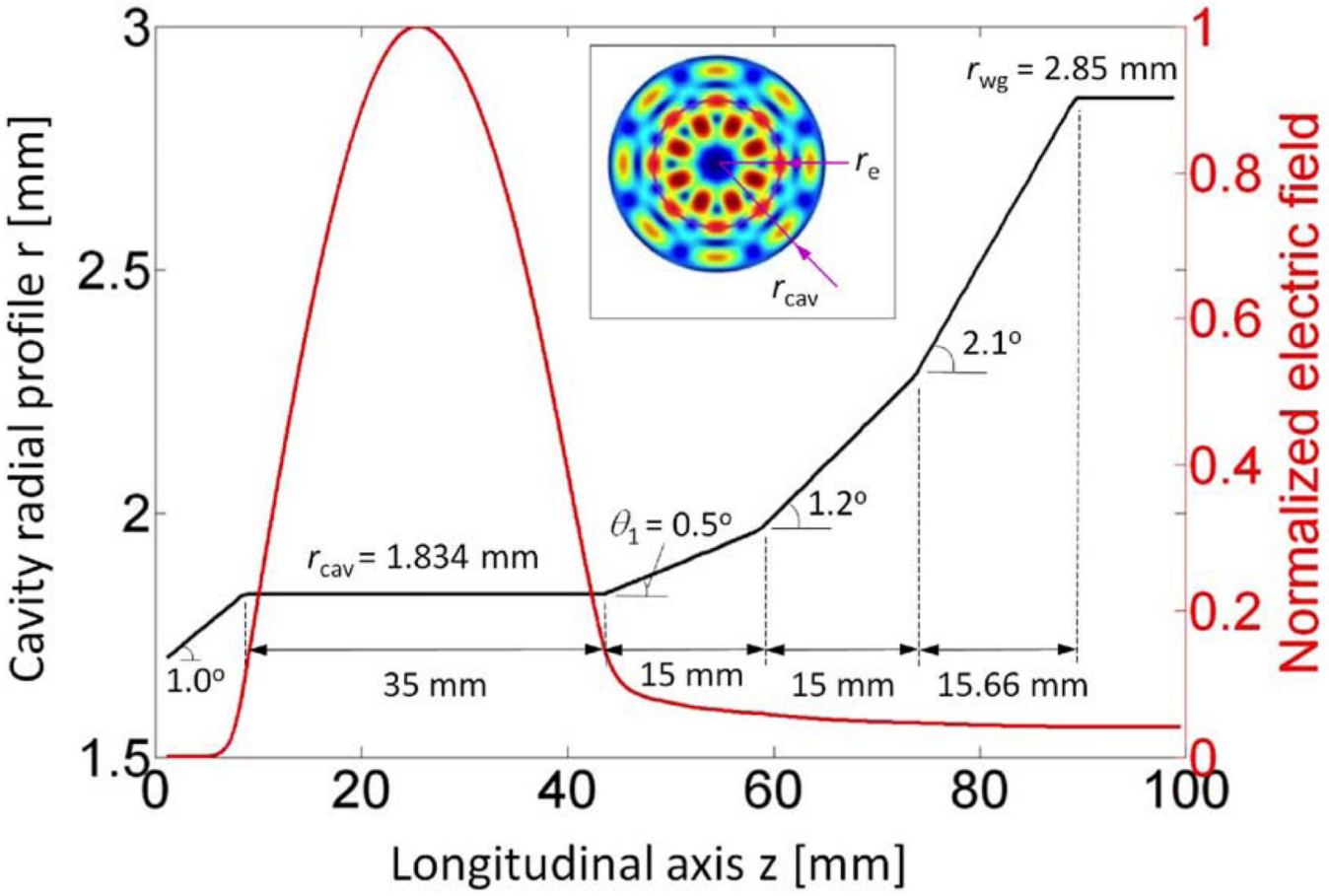

Fig. 8.

Geometrical profile of a cylindrically symmetric 330 GHz gyrotron cavity and the electric field profile of the excited $TE_{4,3,1}$ mode. The insert shows the transverse electric field profile of the cavity mode. The electron beam radius is labeled as r_e. (Adapted from [60]).

Fig. 9.
Photo of the 250 GHz gyrotron oscillator (left), the 380 MHz NMR spectrometer (right).

Fig. 10.
Commercial gyrotron for use in DNP NMR spectroscopy with the magnet shown on the left and the control and cooling systems for the gyrotron shown on the right. (Adapted from [20]).

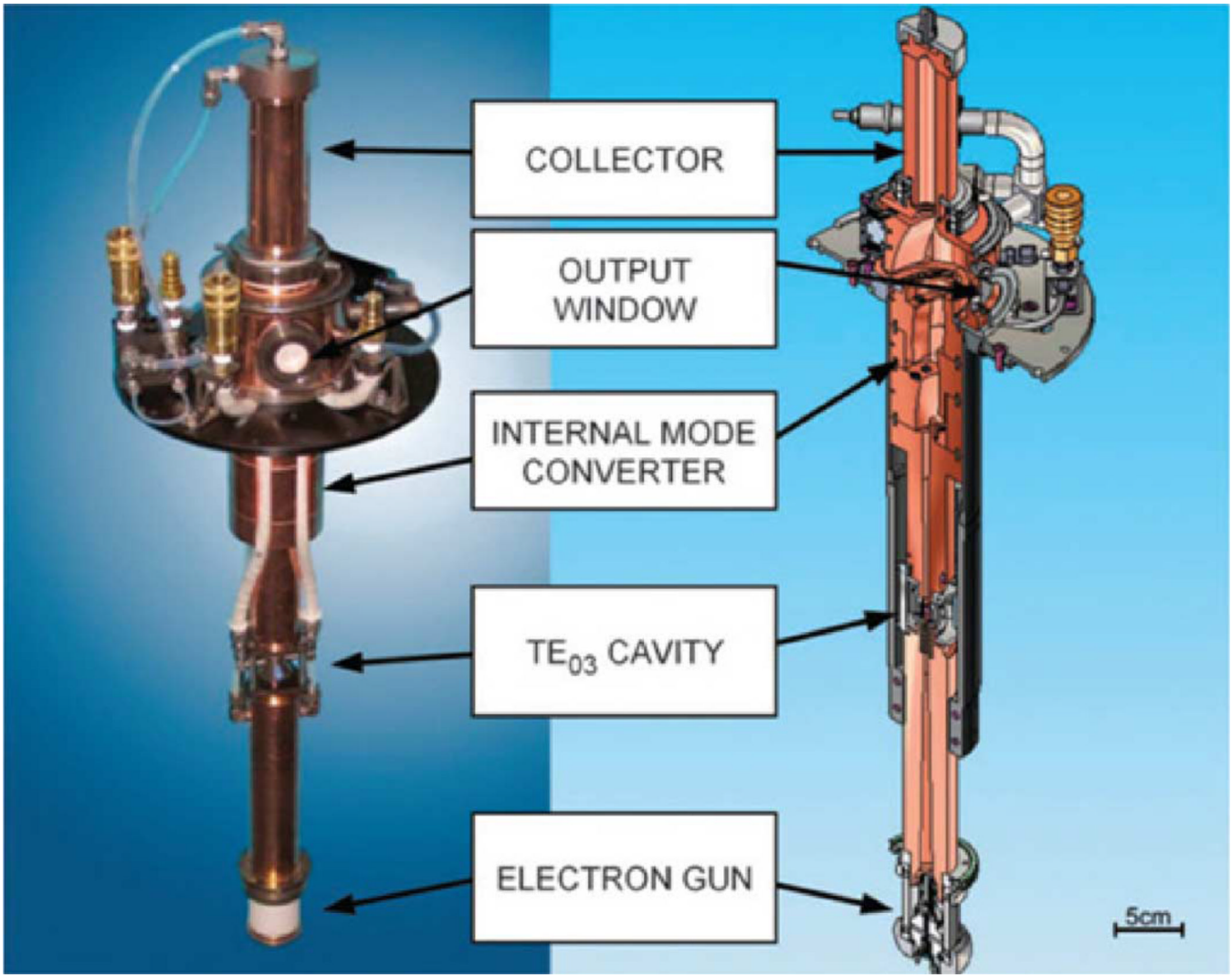

Fig. 11.
Photograph and solid model cross section of the 263 GHz gyrotron tube used in Fig. 10. (Adapted from [20]).

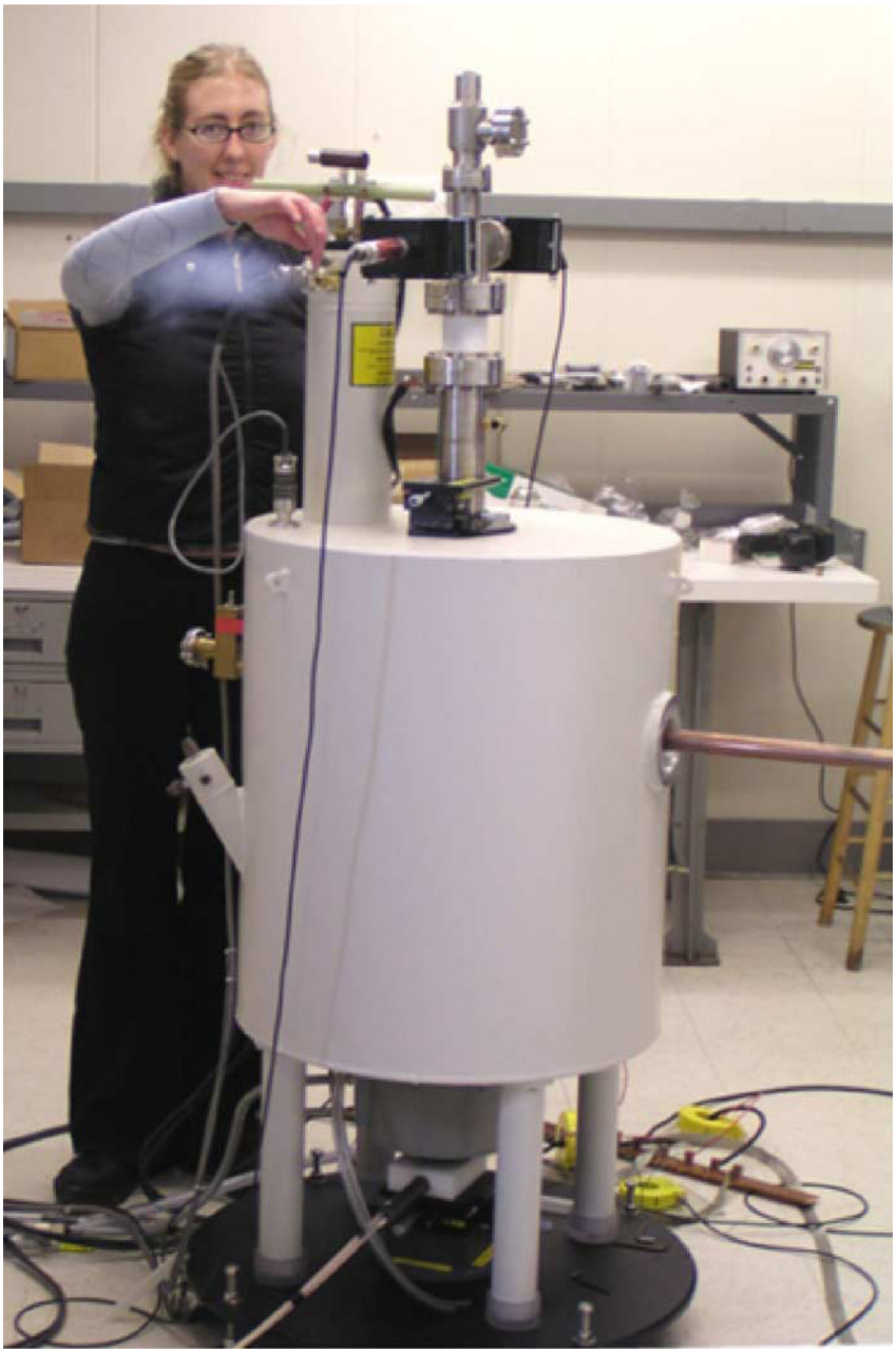

Fig. 12.
460 GHz gyrotron in the superconducting magnet at MIT. (Adapted from [15]).

Fig. 13.
260 GHz Gyrotron Oscillator (left), with overmoded transmission line coupling the THz radiation to the NMR spectrometer (right). Photo courtesy of T. Prisner.

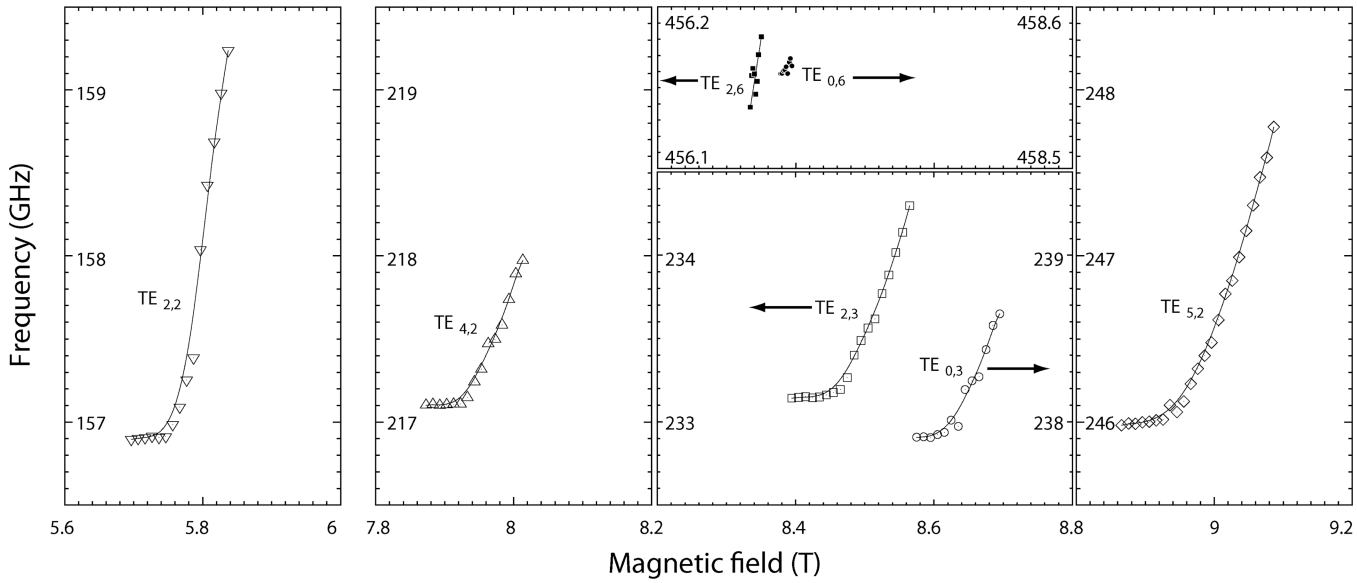

Fig. 14.
First observation of continuous tuning in a DNP NMR gyrotron. (Adapted from [15]).

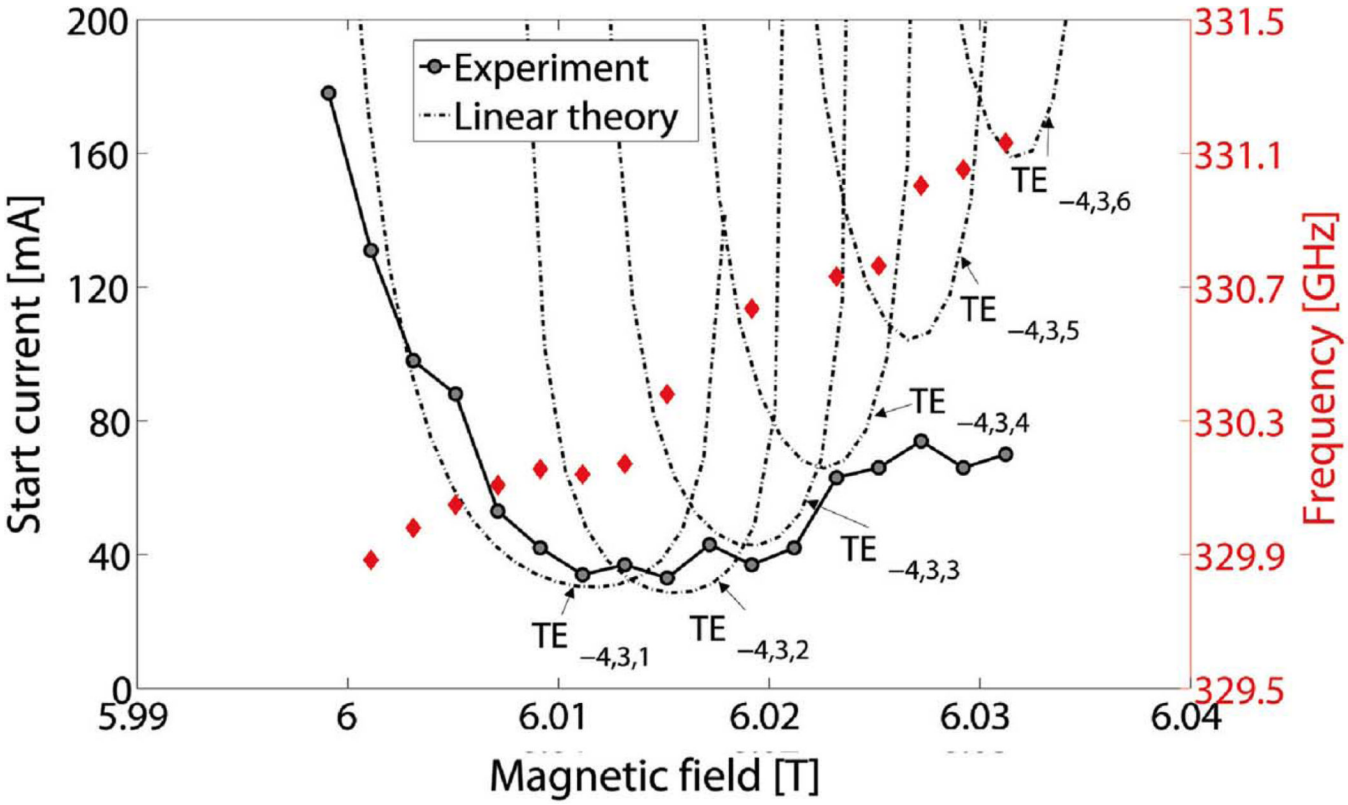

Fig. 15.

Measured start oscillation current (solid line) and measured frequency (diamonds) of the operating mode $TE_{-4,3}$ as a function of magnetic field. The theoretical start currents for the first six axial modes $TE_{-4,3,q}$, where q = 1, 2, 3, 4, 5, 6, are shown as dash-dotted lines and they were computed using linear theory. (Adapted from [60]).

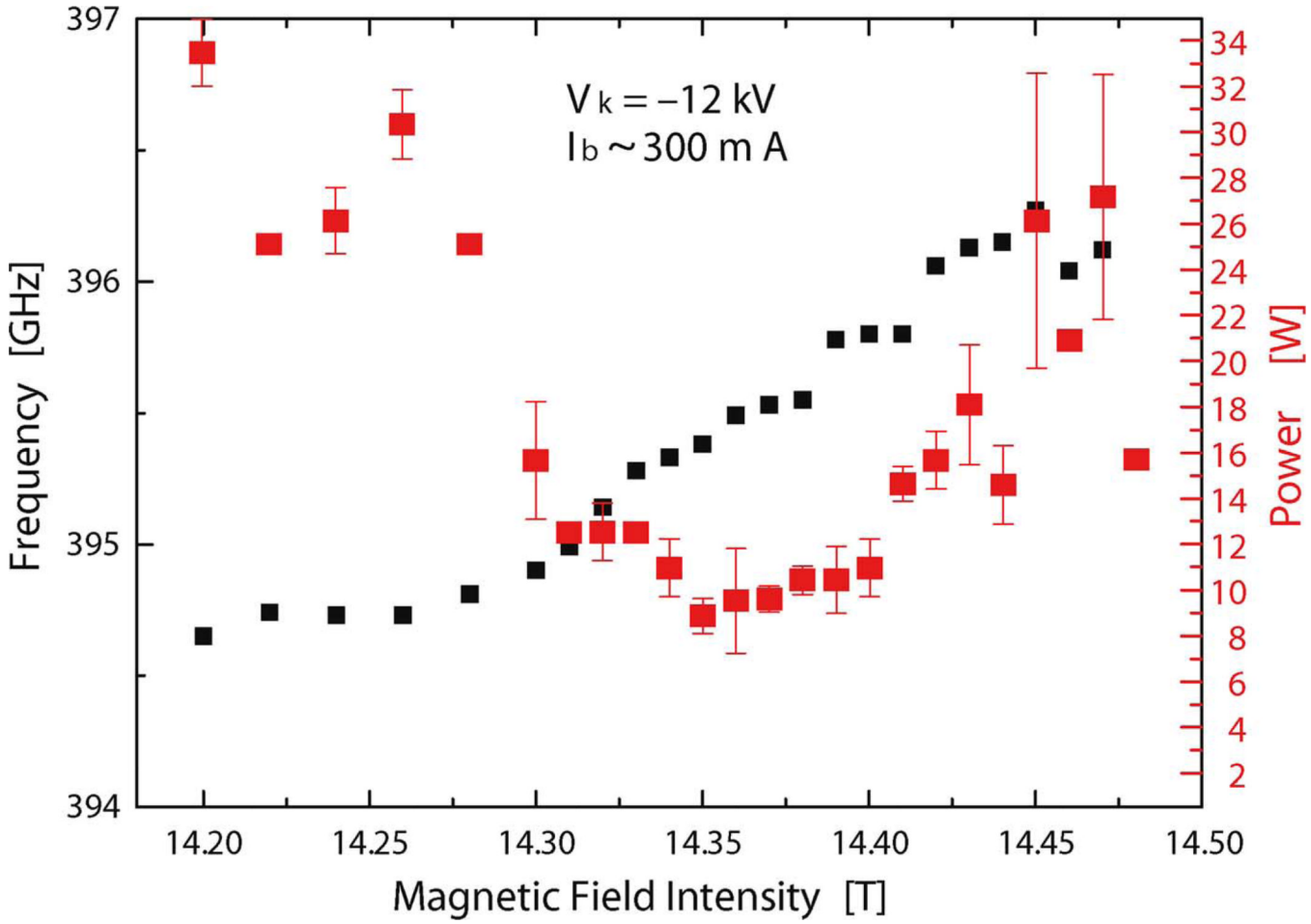

Fig. 16.
Tuning with magnetic field from a 395 GHz fundamental mode gyrotron. (Adapted from [86]).

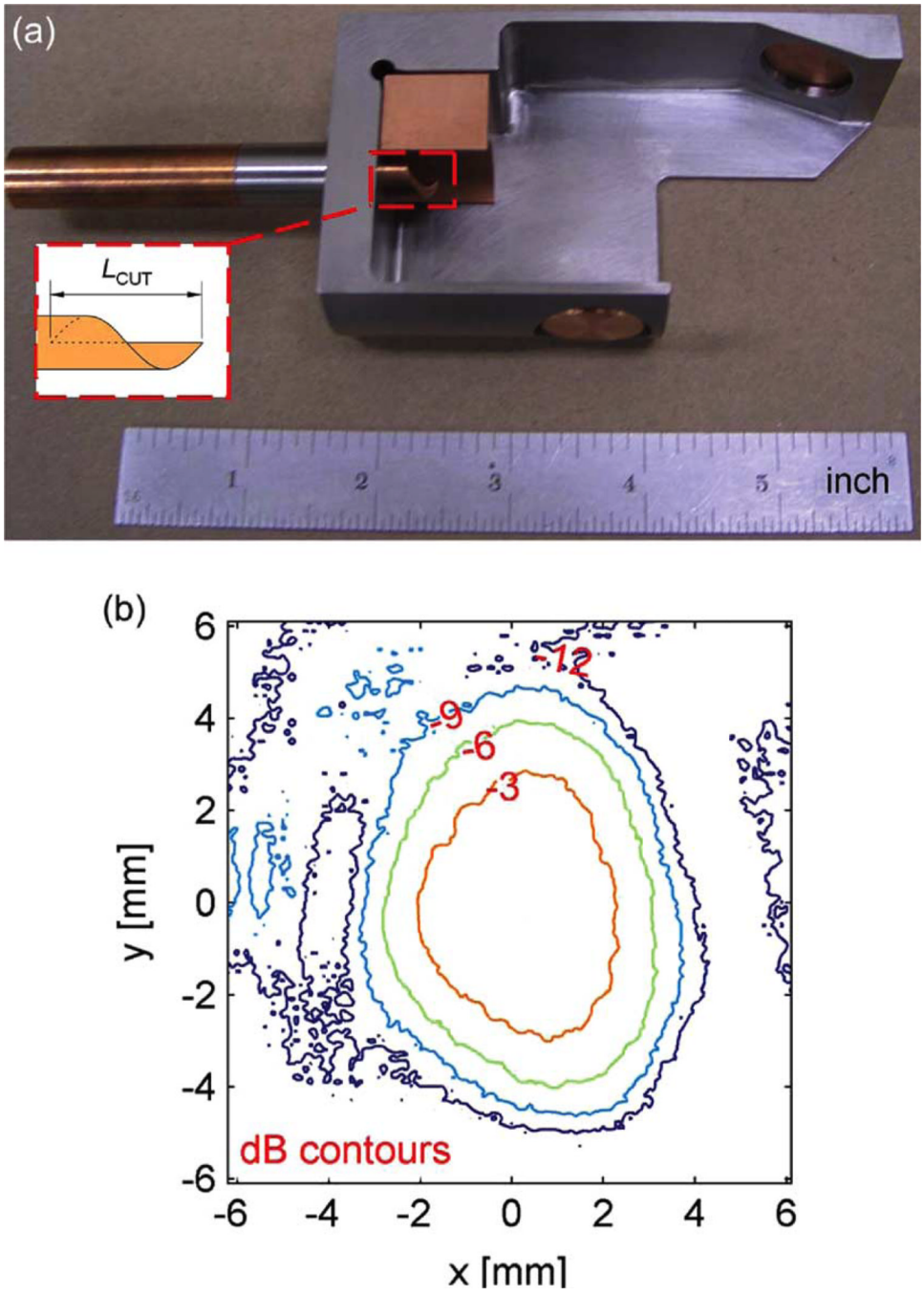

Fig. 17.

(a) Quasi-optical mode converter picture with inset showing the helical launcher orientation; (b) measured profile of the mode-converted $TE_{11,2}$ output beam at the window plane at 460 GHz. (Adapted from [90]).

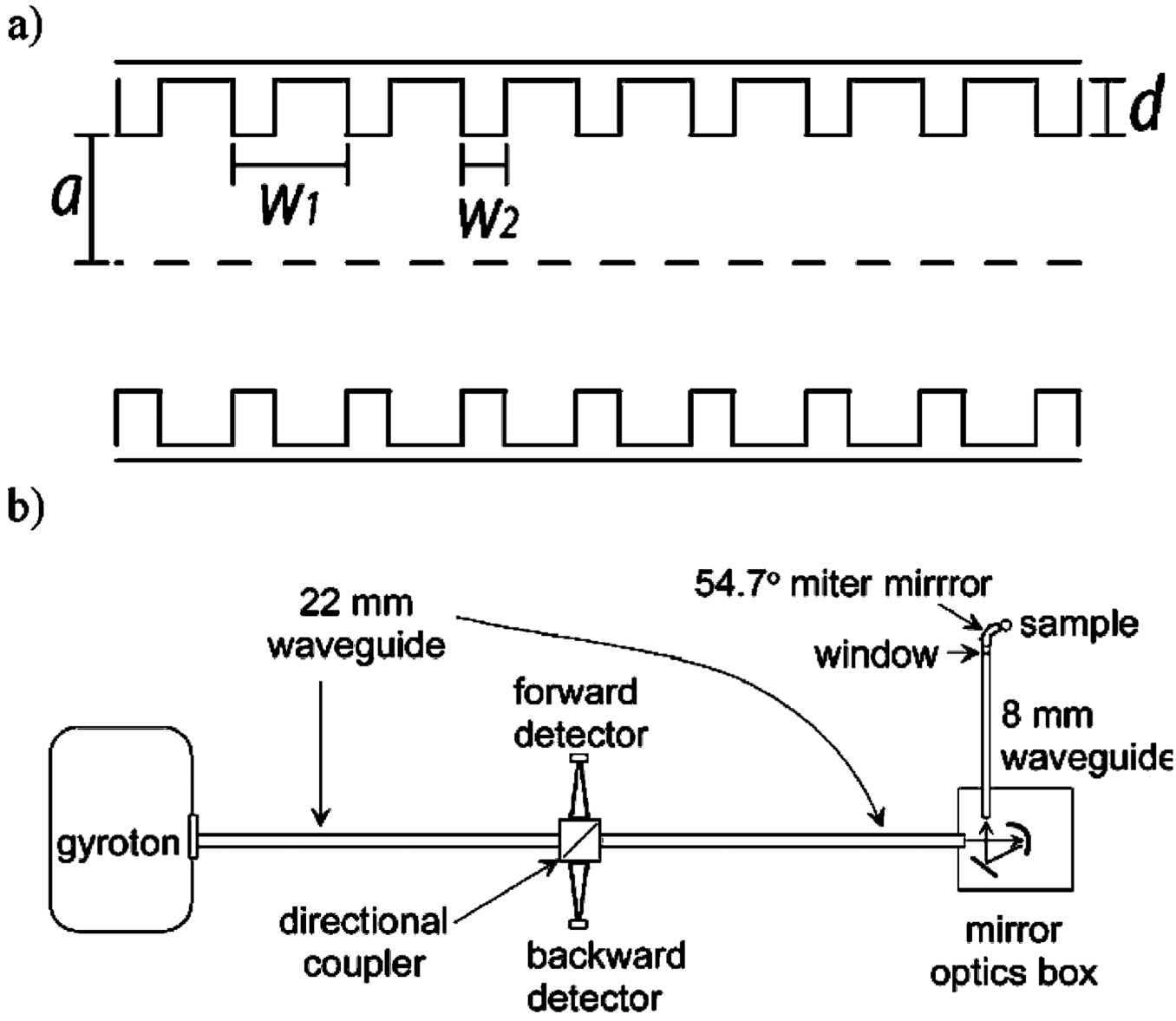

Fig. 18.

(a) Illustration of corrugated metallic waveguide of radius $a \gg \lambda$, groove depth $d \approx \lambda/4$, period $\omega_1 \approx \lambda/3$ and tooth width $\omega_2 < \omega_1/2$. (Adapted from [94]) (b) Schematic of the transmission line used in the MIT 250 GHz DNP NMR system. (Adapted from [81]).

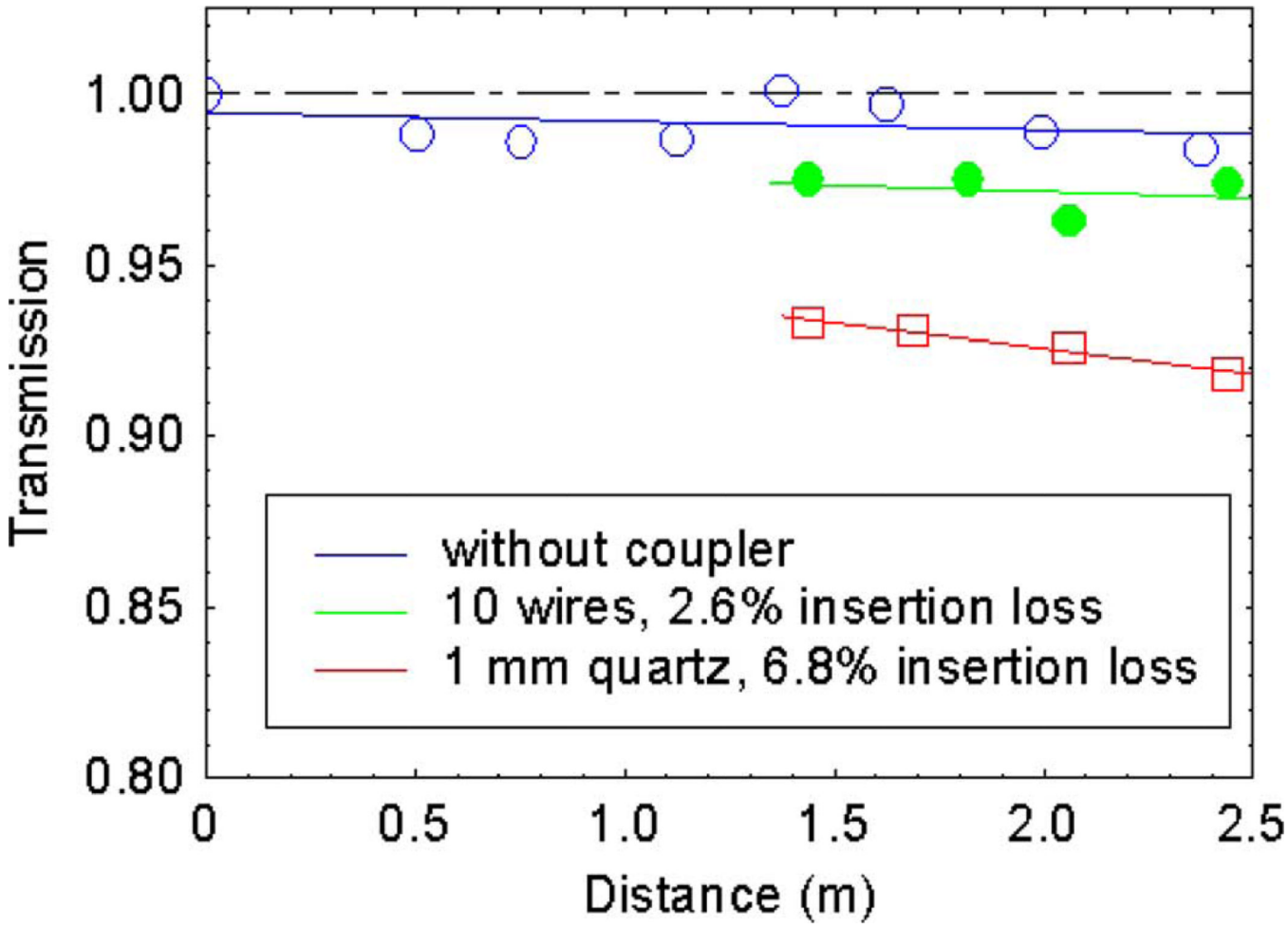

Fig. 19.
Measured loss of the transmission line in Fig. 18. (Adapted from [81]).

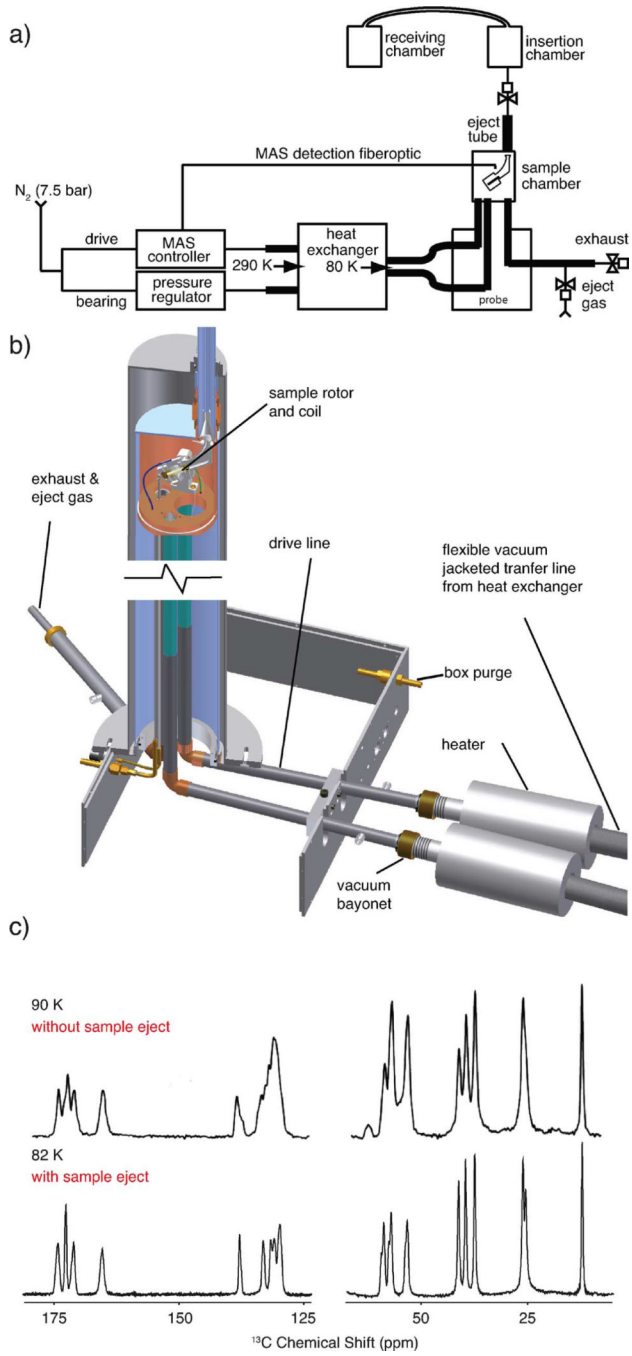

Fig. 20.

Cryogenic MAS and sample exchange. (a) Overview of the system architecture of the cryogenic sample spinning and exchange system. Thick black lines indicate vacuum jacketed transfer lines. (b) Elements of the probe design required from cryogenic spinning. (c) Spectra of a tripeptide with the cryogenic sample exchange and broad unresolved spectrum without the sample exchange. (Adapted from [45], [99]).

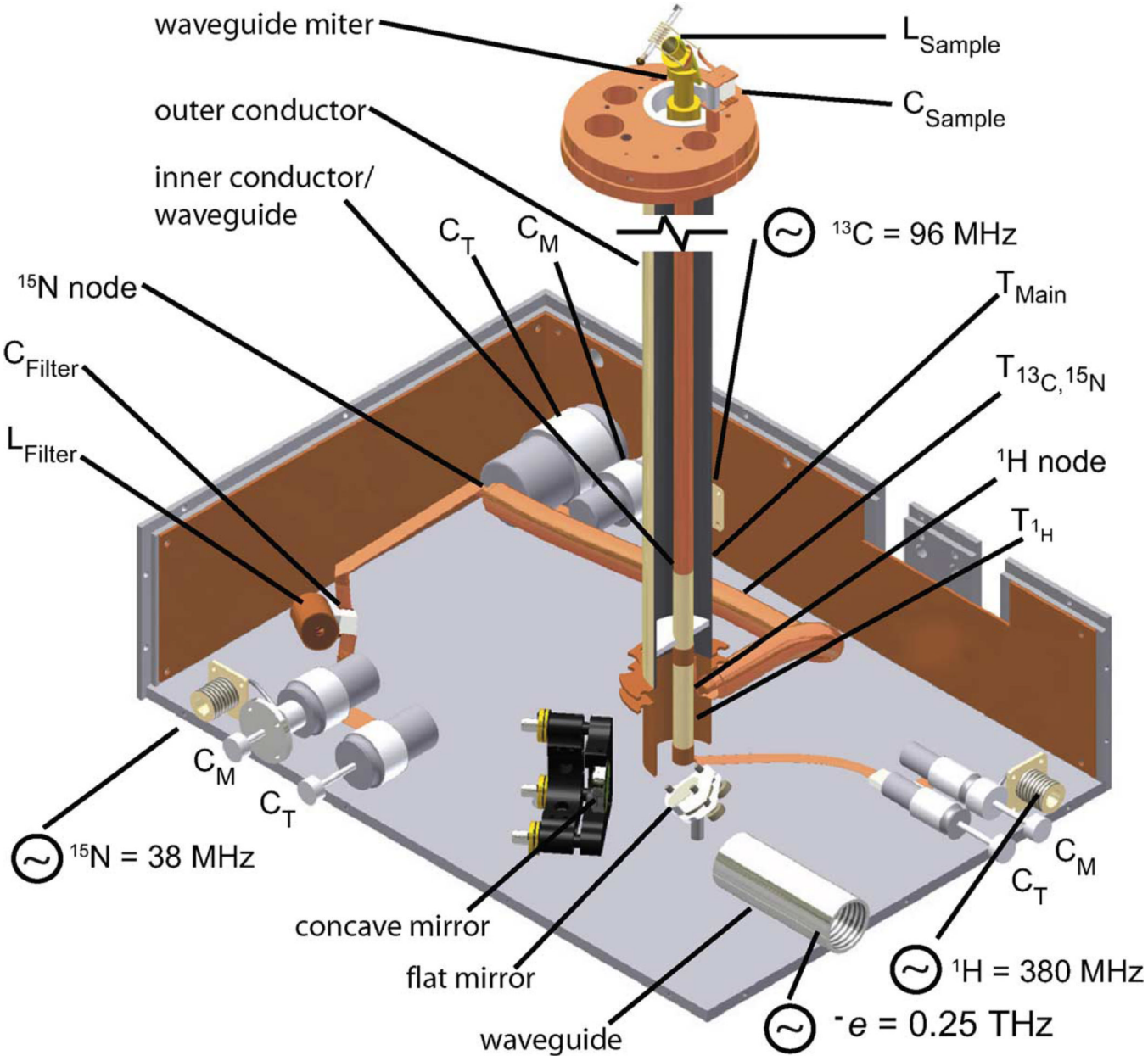

Fig. 21.
Solid model rendition of a typical 4 channel RF-THz circuit showing transmission lines, sample inductor, isolation elements and variable tuning and matching capacitors, corrugated waveguides and quasioptics. (Adapted from [45]).

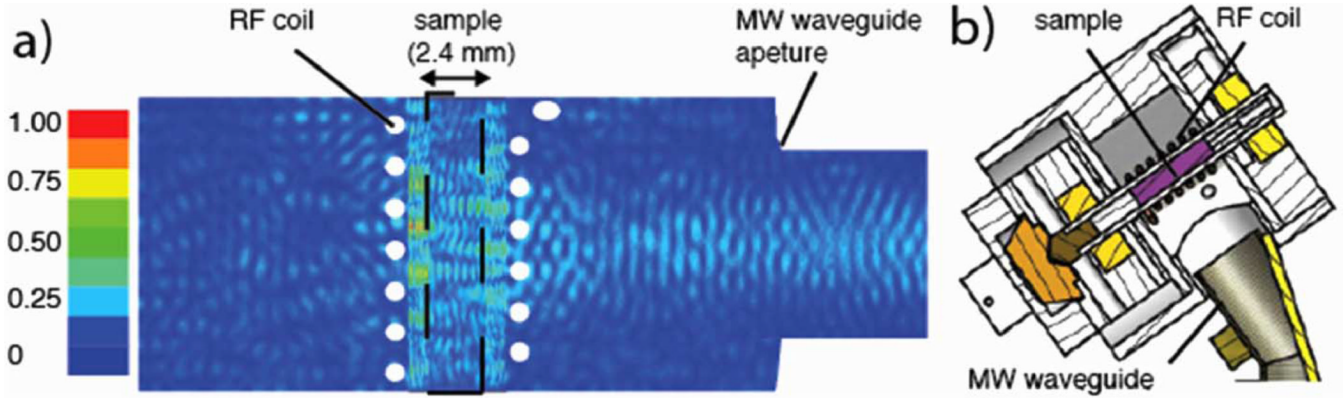

Fig. 22.
THz coupling to sample. (a) HFSS calculation of the THz wave intensity throughout the sample and spinning chamber. (b) solid model depicting the THz antenna, spinning module, and sample. (Adapted from [82]).

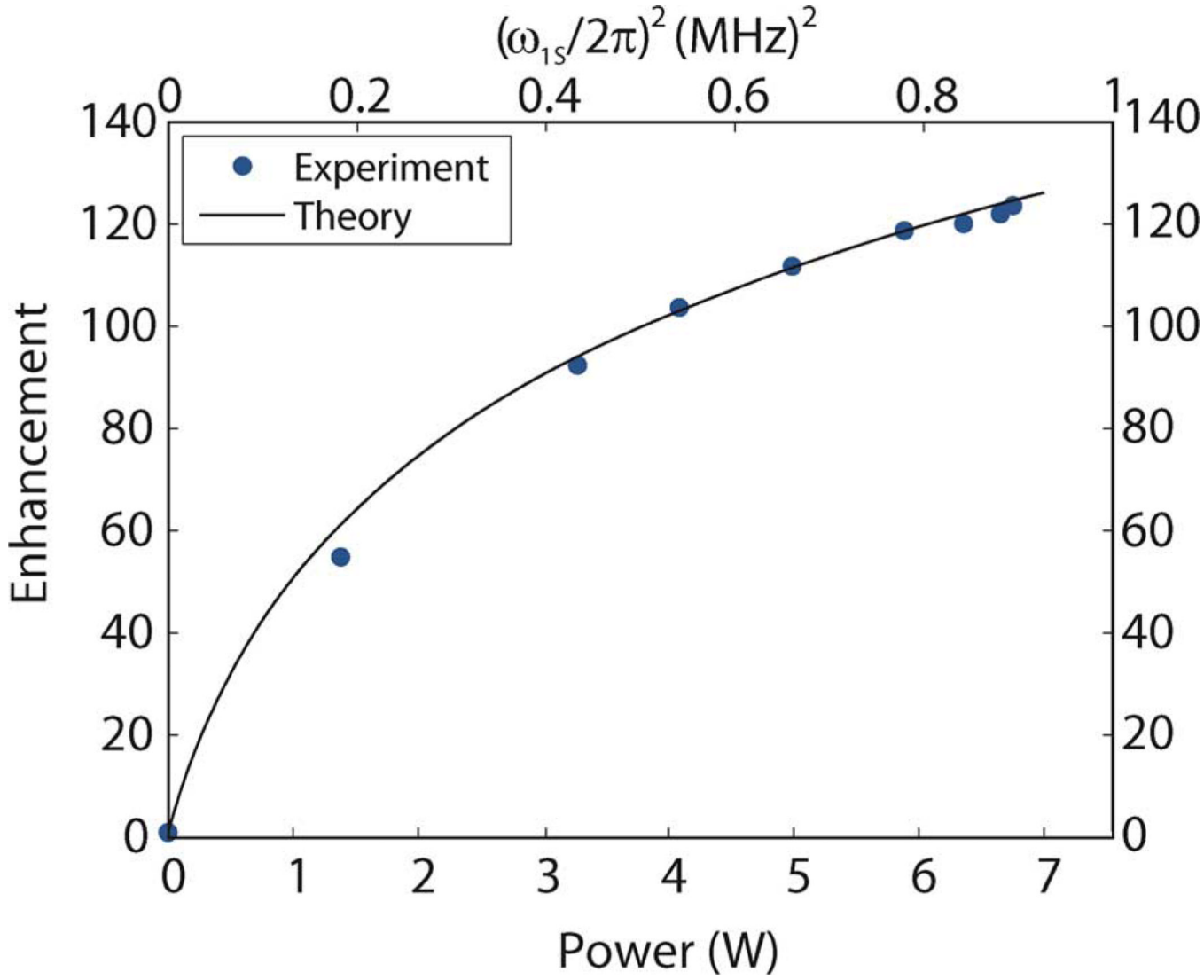

Fig. 23.
DNP enhancement vs. power (bottom) and $\omega_{1S}/2\pi$ (top) for a fully packed rotor of 1 M ^{13}C-urea and 10 mM TOTAPOL dissolved in d_8-glycerol/D_20/H_20 (60/30/10% by volume). (Adapted from [98]).

TABLE I

Requirements for DNP NMR Gyrotrons

Frequency	~28*B_0 GHz (B_0 = NMR field in T)
Output Power	≥ 20 W
Power Stability	±0.5 %
Frequency Stability	< 2 MHz
Run Time	>36 Hours
Lifetime	>50,000 Hours
Voltage Regulation	0.1%
Current Regulation	1%
Output Mode Purity	>90%

TABLE II

140 GHz Gyrotron Parameters

Operating Mode	$TE_{0,3,1}$
Voltage	12 kV
Current	35 mA
Beam Radius	1.82 mm
Output Power	15 W
Magnetic Field	5.12 T
Beam Velocity Ratio ($\upsilon_\perp/\upsilon_z$)	1.6